Global and local analysis of the mechanical and structural characteristics of carotid atherosclerotic plaques for rupture risk assessment.

MSc Thesis in Biomedical Engineering

Pablo de Miguel Muñoz

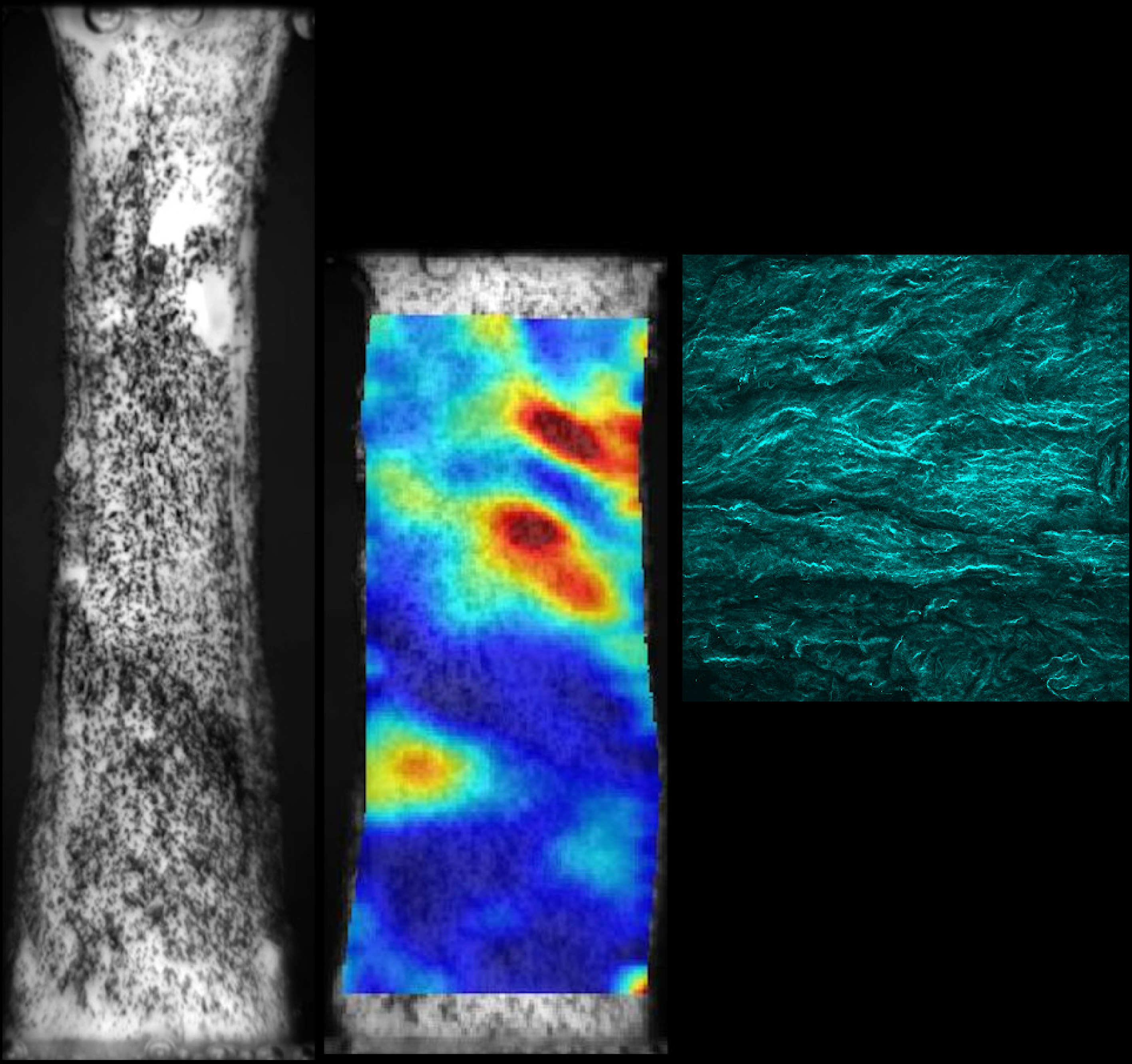

Delft University of Technology

TU Delft

Global and local analysis of the mechanical and structural characteristics of carotid atherosclerotic plaques for rupture risk assessment.

by

Pablo de Miguel Muñoz

to obtain the degree of Master of Science
at the Delft University of Technology,
to be defended publicly on Thursday, February 24, 2022 at 09:30

Student number:	5156084	
Supervisor:	Dr.ir. A.C Akyildiz	TU Delft and Erasmus MC
Daily supervisor:	Ir. S. Guvenir Torun	Erasmus MC
Thesis committee:	Prof.Dr. J. Dankelman	TU Delft
	Prof.Dr. Gijsje Koenderink	TU Delft

Acknowledgments

This project, which was a part of the BME master's at TU Delft, has allowed me to investigate atherosclerosis in depth, one of the most "important" and widespread diseases worldwide. The project was performed in a leading hospital in the Netherlands and in Europe, as it is the Erasmus Medical Center, and I am really grateful for the opportunity given. It has been a tough and challenging project, especially given the COVID situation of the past year; but it has permitted me to grow a lot as a biomedical engineer and as a person. The fact that it has been so arduous, makes me to be more grateful and value way more the people that have surrounded me and have helped me along the way. I would like to start by thanking Professors J. Dankelman and G. Koenderink for agreeing to be on the committee of this thesis.

I would like to thank my supervisor, Ali Akyildiz, for guiding me and for being extremely helpful. Also, for trusting me and allowing me to perform these very promising experiments, which will provide great advances, I am sure. I really admire his way of transmitting knowledge and debating about scientific topics, which makes them seem to be way easier than what they are in reality. I would also like to thank Su Guvenir, for being the best lab mate someone can have. Together, we faced a lot of difficulties in the experiments, but we only needed a Happy Meal to solve them, or at least, to make us forget about them for a bit of time. I am sure that after this project, we'll keep in touch for many years. I would also like to thank Robert Beurskens, for all his help, basically being the only person I could meet during my first two months at the hospital, and for showing me a huge amount of bad jokes (which are the best). I really appreciated the support and company from Hanneke Crielaard, especially for bringing such an energy to the lab that made me dance even on the worst days. In addition, I would like to thank Frank, Rachel, Manouk, Jo-anne and Madusha. In general, I much appreciated everyone's company and support at the Cardiovascular Biomechanics department in Erasmus MC. There is such an amazing team there.

I am also really grateful for all the friends I have made in Delft; Luis, Alberto, Amaia, Nuria, Alvarito, Karl, Chu-Hsuan, which have made the path easier. I also want to thank my friends from Spain, which motivated me to finish by sending pictures of the sun.

But especially, I want to thank Nati and my family; I would not be where I am right now without them. I just hope I could give back the support that I received from them.

Pablo de Miguel Muñoz
Delft, February 2022

Abstract

The rupture of atherosclerotic plaques present in vital arteries is the main trigger of fatal cardiovascular events, such as heart attacks and strokes. Plaque rupture is a mechanical failure of the fibrous plaque tissue that ensues upon large deformations of the tissue, induced by the blood pressure. Current knowledge on the rupture characteristics of plaque tissue is, however, scarce and limited to global, aggregate tissue properties, although plaque rupture is a local phenomenon. Hence, local mechanical and structural evaluations of the heterogeneous, highly collagenous plaque tissue are required for better understanding the plaque rupture.

To achieve this, a combination of mechanical and structural analyses was performed in this study. The collagen structure of human carotid plaques was imaged by means of Multiphoton microscopy using Second-Harmonic generation signals (MPM-SHG), and it was characterized in terms of fiber orientation and dispersion. Subsequently, the imaged plaques were subjected to uniaxial tensile tests until rupture to characterize their mechanical response. Apart from the traditional global analysis, the local mechanical response was analyzed through Digital Image Correlation (DIC). This way, the structural heterogeneity of the plaque tissue was assessed and the role of collagen fiber organization in plaque mechanics was investigated locally.

The structural analysis of the plaque tissue samples demonstrated a predominant overall fiber orientation along the circumferential direction of the artery. Yet, high local variability in collagen orientation and dispersion was measured. The global, average mechanical response of the plaques showed a non-linear behavior, typical to many soft biological tissues and the local mechanical analysis demonstrated highly heterogeneous strain distributions in the plaques. Furthermore, regions that were about to rupture, showed higher tensile strains compared to the overall plaque strain, implying the possibility of establishing strain as a predictive metric for rupture. Whereas the global analysis did not yield any important correlation between the overall collagen structural parameters and the global mechanical tissue response, the local analyses indicated that the regional predominant fiber angle might influence the regional strain, and probably the plaque rupture risk.

Contents

Nomenclature

Abbreviations

Abbreviation	Definition
CEA	Carotid Endarterectomy
DIC	Digital Image Correlation
FOV	Field of View
GL-based	Gauge length-based
MIP	Maximum Intensity Projection
MPM-SHG	Multiphoton Microscopy with Second-Harmonic Generation
ROI	Region of interest (DIC)
SALS	Small Angle Light Scattering
SMCs	Smooth Muscle Cells
UTS	Ultimate Tensile Strength
USR	Ultimate Stretch ratio
WL	Width-to-Length Ratio

Symbols

Symbol	Definition	Unit
μ_p	Predominant fiber angle [-90°+90°]	[°]
μ_{pcirc}	Predominant fiber angle difference to Circ. [0°+90°]	[°]
σ_p	Standard deviation (Gaussian fitted)	[°]
P_{ani}	Anisotropic fraction [0 1]	
DI	Dispersion index [0 1]	
λ	Stretch Ratio	
ε	Green-Lagrange strain	
σ	Cauchy stress	[MPa]

List of Figures

1

Introduction

1.1. Background

Cardiovascular diseases (CVDs) are the primary cause of death globally, taking an estimated 18 million lives each year, which accounts for 31% of all deaths [1]. Four out of five CVD-related deaths are caused by heart attacks and strokes, which are triggered by atherosclerosis in a vital artery, such as carotid or coronary. Atherosclerosis is a chronic immunoinflammatory disease of the vascular system that entails a progressive thickening of the arterial wall due to the formation of the so-called plaques [2][3].

A healthy artery consists of three structural layers: the adventitia (outermost), made up of connective tissue that provides structural support and shape, the tunica media (middle layer), consisting of connective tissue and smooth muscle cells (SMCs) that handle the blood pressure, and a thin tunica intima (innermost), mainly comprised of an endothelial layer bordering with the bloodstream [4].

Atherosclerotic plaque formation starts in a healthy artery with a fatty streak, when the dysfunction of the endothelial layer permits the migration of low-density lipoproteins (LDLs) to the intima layer. Here, the oxidative modification of LDLs induces the infiltration of monocytes and T-cells, initiating an immune response. The progressive development of plaques is caused by the accumulation of lipids and the aggravation of the inflammatory response. In addition, the SMCs of the media layer are recruited in the defective area. SMCs proliferate and fabricate a dense extracellular matrix, mainly composed of collagen fibers, which surrounds the lipid core resulting in a fibrous plaque (Fig. 1.1). The layer of fibrous connective tissue at the luminal side of the wall is known as the fibrous cap, which seals the plaque components from the blood stream. The collagen-rich matrix confers strength and stability to plaques [5][3]. With plaque progression, the deposition of macrophages and SMCs along with the lipids and lipid-engorged cells constitute a growing necrotic core below the extracellular matrix. The collagenous plaque network integrity can be then weakened by T cell mediators, such as IFN, which can affect the ability of the SMCs to synthesize interstitial collagen. Furthermore, activated macrophages producing matrix metalloproteinases (MMPs) contribute to the degradation of collagen. Besides, calcifications can arise in the plaques due to a dysregulation of calcium mineral deposition and impaired clearance. The calcium aggregation deposits can convert to large nodules in the plaques [2][6][7][8].

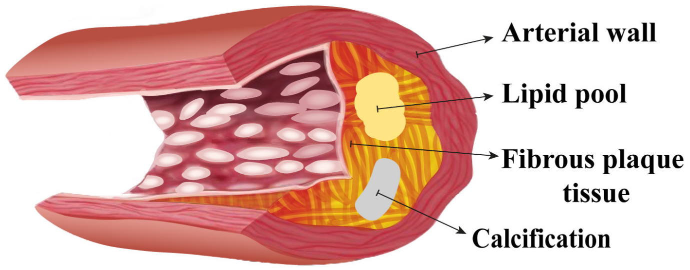

Figure 1.1: Atherosclerotic plaque in an artery with macroscopic components highlighted.

Even though plaques could be enlarging over decades in several locations, atherosclerosis remains asymptomatic during most of its slow progression. Eventually, and only when there is a severe lumen narrowing or a plaque rupture, acute cardiovascular events emerge, whose effect depends on the plaque location (*e.g* ischaemic stroke due to plaque in carotid artery or myocardial infarction due to plaque in coronary). Of these two triggers (lumen narrowing and plaque rupture), the leading cause of the acute syndromes is the plaque rupture [6][9]. Plaque rupture induces thrombosis when the plaque material within the arterial wall comes into contact with the blood [3][2].

The classic and most widespread criterion for assessing the clinical significance of atherosclerotic plaques is the degree of luminal stenosis, i.e. the proportion of lumen narrowing. However, this criterion is being questioned nowadays, as it does not address the rupture risk of a plaque [6]. Therefore, identifying which plaques are prone to rupture is an active research field [10]. There is an urgent need to broaden our understanding of plaque vulnerability and the rupture mechanisms in depth, in order to improve the rupture risk assessment and the planning of effective treatments.

1.2. Motivation

The plaque rupture event depends on many interrelated factors and complex biological processes, but in the end, it is fundamentally a mechanical failure of the fibrous plaque tissue. The intraluminal blood pressure, which is the predominant mechanical loading in the arteries, causes considerable deformations that induces high stresses in the plaques and can make them lose their structural integrity [9].

In this context, the biomechanical analysis of atherosclerotic tissues can provide important knowledge about the disease and aid to improve diagnosis, prognosis in the form of rupture risk assessment, and treatment, by easing the development of patient-specific treatments. Computational models such as finite element models can serve as great tools for predicting atherosclerotic tissue mechanical behavior and allow the simulation of interventional therapies. Nonetheless, their predictive accuracy depends on the correct representation of plaque mechanics, of which there is still limited knowledge. In other words, for being able to correctly use these models and understanding the mechanisms that govern rupture, the precise mechanical characterization of plaque tissues is essential, which is done through experimental mechanical testing *ex vivo* [9][11].

To determine the mechanical properties of biological tissues *ex vivo*, a widely employed experimental method is the uniaxial tensile testing, during which, the specimens are stretched in a single direction and the induced stress is quantified [12]. This technique, along with other traditional mechanical tests treats the samples as continuum bodies, and therefore, current literature on plaque tissue mechanics typically reports average properties based on the homogeneity assumption [10][13].

However, atherosclerotic plaque tissue is highly heterogeneous in structure (cellular, fibrous, lipid components and calcifications [3][2]). Since the mechanical properties of the biological tissues are dependent on the microstructural integrity of all their constituents, the assorted composition of atherosclerotic plaques is likely to lead to a strong heterogeneity in their mechanical properties. This explains the large variation in mechanical results reported by several studies, which performed global analyses and did not examine plaque's phenotype. Consequently, there is a need for extensive investigations on the contribution of individual plaque constituents to mechanics [10]. Furthermore, since plaque rupture is a local event, local approaches for the evaluation of mechanical and structural properties have the potential to provide better insights in the search for a better risk assessment, as they could properly address the heterogeneity of the tissues [14][11][9][10][15].

Among all the constituents, collagen is the main load-bearing component of many biological tissues, including arteries. Upon pressure increase, collagen fibers straighten and are recruited to carry the load (Fig. 1.2). Therefore, the organization and state of collagen fibers maintain the function, integrity and strength of arteries, being responsible for their stiffness and anisotropic mechanical behavior [16][15][17].

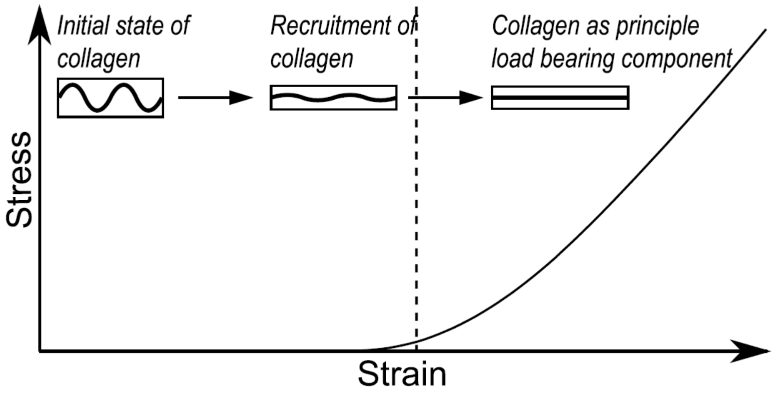

Figure 1.2: Mechanical behavior of collagen under tension. From [17].

As in healthy arteries, fibrillary collagen is also abundant in atherosclerotic plaques (up to 60% of the total protein [5][18]) and therefore, its organization is likely to determine the mechanical properties of the plaque [19]. In this regard, the influence of collagen content on plaque mechanics has been investigated by different groups; some of which stated that it is positively correlated to local stiffness [20][21], fibrous cap's mechanical strength [22] and plaque stability to delamination [23], and negatively correlated to plaque toughness [24]. On the other hand, the data about collagen architecture (orientation and dispersion) in human atherosclerotic plaques is rather scarce [18][15][22], and there has been only one study where the collagen orientation was related to the mechanical properties of the plaque. In this study, *Johnston et al.* observed that the gross collagen fiber orientation relative to the loading direction determined the gross elastic mechanical properties in the fibrous caps, suggesting the critical role that collagen architecture can have in plaque rupture [11]. Nonetheless, that only study does not provide enough information about the influence of collagen fiber orientation and dispersion on plaque mechanics, in terms of local and rupture properties. Therefore, further *ex vivo* experiments, where the characterization of local collagen microstructure can be combined with mechanical tests, are needed for elucidating more about the mechanical behavior and rupture mechanisms of atherosclerotic plaques.

1.3. Aims of the study

The motivation of this project is to better understand the atherosclerotic plaque rupture event, by characterizing the local and global mechanical and collagen microstructural properties of atherosclerotic plaques and investigating their possible correlations. The main goals are as follows:

- Characterize the collagen structural properties of carotid atherosclerotic fibrous plaque tissues, in terms of local collagen fiber orientation and dispersion.
- Subject the imaged plaque tissues to mechanical tests for characterizing their global and local mechanical responses at failure and pre-failure.
- Investigate the relation of the collagen structural properties to the local and global mechanical responses of the tissue.

2

Materials and Methods

2.1. Outline of the experiments

In this experimental study, the mechanical tests were conducted on carotid endarterectomy (CEA) samples. The methodology, which is detailed in this chapter (overview in Fig. 2.1), is organized into four main parts:

1. Tissue preparation: Following the collection of the excised CEA samples, μCT scans were performed for examining the overall structure of the specimens to identify calcifications. Using this information, non-calcified rectangular CEA strips were dissected for mechanical tests.
2. Collagen imaging: The collagen fiber structure of the luminal side of the CEA strips was imaged under Multiphoton microscopy using Second-Harmonic Generation signals (MPM-SHG). The data analysis of the acquired stacks of images allowed extracting collagen structural properties in the form of predominant fiber angle (orientation) and dispersion.
3. Mechanical testing: The non-calcified rectangular CEA strips were tested under uniaxial tensile testing conditions in the circumferential direction of the artery in a custom-designed set up. The global mechanical responses of the strips were studied focusing on pre-failure (inflection point and stiffness) and failure (ultimate parameters) behavior through traditional methods. Ultrasound imaging was performed to accurately determine the thickness of the samples.
4. Digital Image Correlation (DIC) analysis: DIC was performed on the images taken during the tensile tests and permitted the generation of the full-field strains at the luminal surface of the strips for its local mechanical analysis (deformation), in search for rupture strain patterns (or fingerprints).

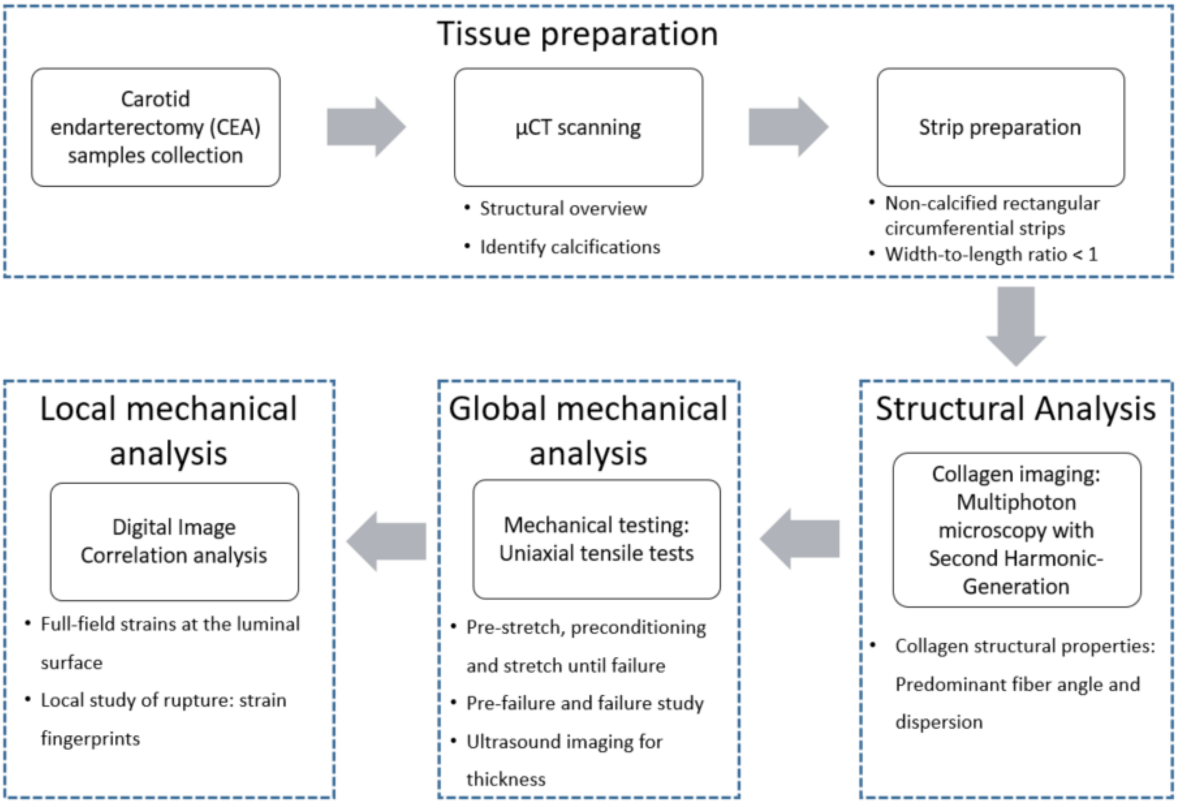

Figure 2.1: Overview of the project's methodology.

2.2. Samples Collection

Human carotid atherosclerotic plaque samples were acquired at the Erasmus Medical Center, (Rotterdam, the Netherlands), from consenting patients who underwent carotid endarterectomies; a surgical operation in which the atherosclerotic plaque is removed from the artery (Fig. 2.2) [25]. This procedure was approved by the hospital's Ethical Research committee. After excision, the samples were snap-frozen and preserved at -80°C until the day of imaging. The mechanical properties of the samples were assumed to not be effected by this freezing protocol [26]. In total, 19 CEA samples were used in this project.

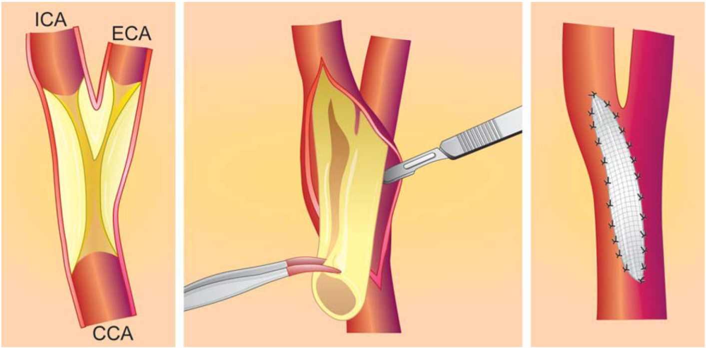

Figure 2.2: Technique of carotid endarterectomy. From [27].

2.3. µCT scanning

µCT scans were performed to provide 3D structural overviews of the excised CEA samples, which allowed identifying the location and morphology of calcifications. They permitted their exclusion when dissecting rectangular strips for the mechanical tests. Calcifications were avoided as they have been found to affect the stiffness, strength, toughness and rupture initiation of plaques [28][24][29], and the aim of this project was to investigate the mechanical properties of the highly collagenous plaque tissue and the association of these properties to the underlying fibrillary collagen structure.

On the day of imaging, CEA samples were equilibrated to room temperature and scanned on a µCT imaging system (Quantum GX2, PerkinElmer, USA) using an X-ray filter of Cu 0.06 mm + Al 0.5 mm, in dry conditions (Fig. 2.3A). All the scans were operated at 90 kV and 88 mA, over a field of view of 86 mm, a rotation of 360 degrees, for an acquisition time of 4 minutes. A scan resolution of 172 µm (voxel size) was achieved, so the system detected calcified particles larger than $5x10^{-3}mm^3$. Subsequently, samples were again snap-frozen in liquid nitrogen and maintained at -80°C until the day of the collagen imaging and mechanical testing. According to *O'Reilly et al.*, who also performed µCT scans before uniaxial tensile tests, this imaging process should not have a significant effect on the mechanical response of the samples [30].

Scans were exported as DICOM files for a subsequent image analysis in 3D Slicer (version 4.11) Within this software, µCT slices were segmented into two parts, non-calcified plaque tissue and calcifications, by using the threshold tool to set Hounsfield Unit ranges of -700 to 449 HU, and 450+ HU, respectively. The segmentation of the calcifications was possible due to the high attenuation of the X-ray emitted by the scanner, which supposed a high contrast with respect to the rest of the tissue [24]. Finally, 3D reconstructions of the CEA samples (Fig. 2.3B) were generated to check the samples' structure, calcification distributions, and dimensions for strip dissection.

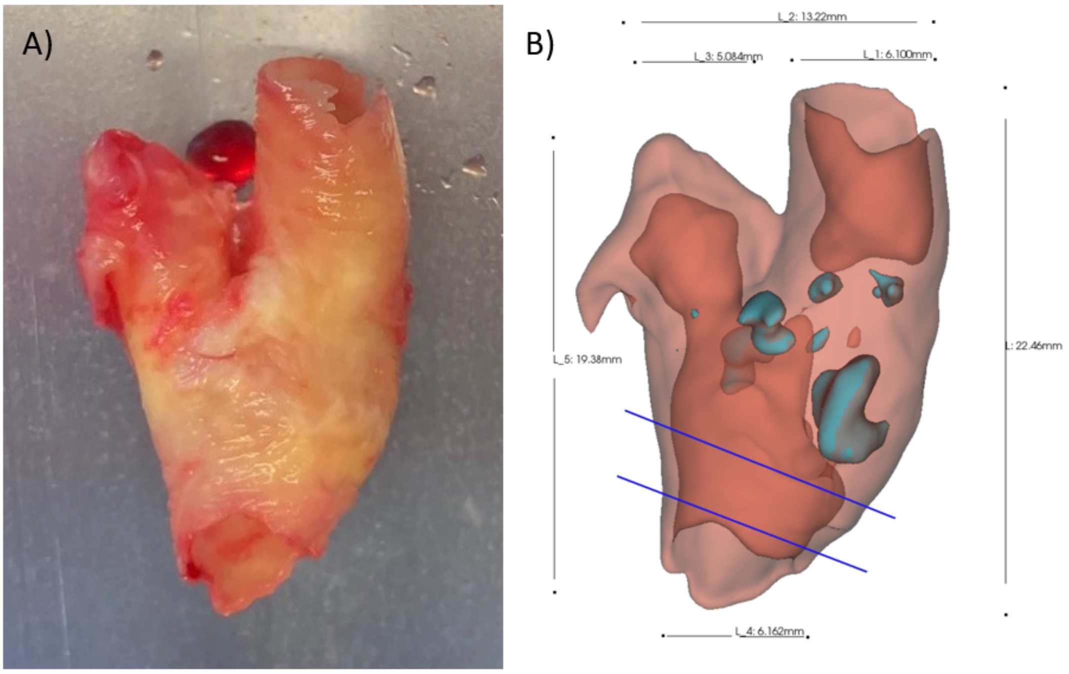

Figure 2.3: A) CEA sample on the µCT platform before imaging. B) Reconstructed µCT scan showing non-calcified tissue (red) and calcified constituents (light blue) and their dimensions. The blue lines enclose the area to provide the location of the strips obtained.

2.4. Strip preparation: Tissue dissection

On the day of testing, each plaque sample was equilibrated to room temperature by submersion in phosphate buffer solution (PBS). Prior to MPM-SHG and uniaxial tensile testing, each CEA sample was dissected to obtain rectangular circumferential strips, *i.e.*, being the long axis oriented towards the circumferential direction of the artery. In order to achieve this, the specimens were cut open along the longitudinal axis of the artery using surgical scissors and tweezers (2.4). They were folded open, exposing the luminal side (i.e., intimal layer) up, and the approximate geometry was measured using a ruler to decide the dimensions of the strips. The selection of the tissue piece to be cut was supported by the 3D reconstructed μCT images, focusing on avoiding areas of calcifications. Moreover, any tissue area that appeared to be damaged was discarded.

From the selected areas, rectangular non-calcified strips (Fig. 2.4) were dissected with certain dimensions that permitted to have a width-to-length (WL) ratio < 1 in the gauge length once these were mounted in the tensile tester. Therefore, strips were suitable for appropriate tensile tests in terms of boundary conditions (as opposed to planar shear tests), according to *Mulvihill et al.* [28]. After cutting the specimens, the dimensions of each strip, including thickness, were measured at different points with a ruler. In addition, photographic images were taken to measure their dimensions *a posteriori*, by calibrating them in ImageJ (NIH, USA). The lengths, widths and thicknesses of the excised strips ranged from 10 – 25 mm, 2 – 6 mm, and 0.5 – 2 mm, respectively. Note that the length stands for the circumferential direction of the arteries (the testing direction), and the width stands for the longitudinal (or axial) direction. Out of each sample, between 1 and 3 strips were obtained. In total, 31 rectangular circumferential non-calcified strips from 19 CEA samples, and hence, patients, were tested.

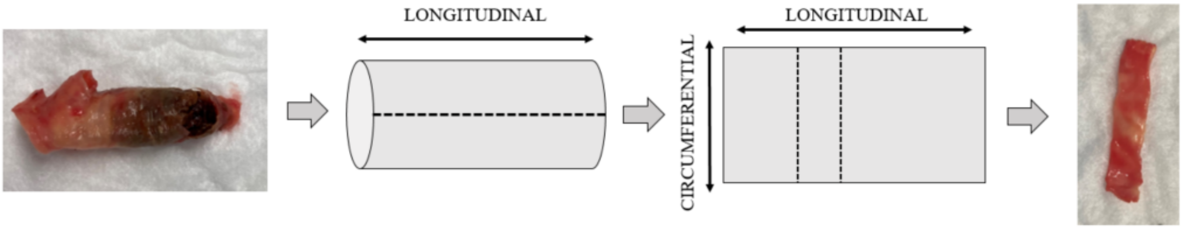

Figure 2.4: Dissection of a CEA sample. Circumferential non-calcified strips were obtained for MPM-SHG imaging and uniaxial tensile tests.

2.5. Collagen imaging: Multiphoton microcopy and Second-Harmonic Generation

Multiphoton microscopy was employed to capture the 3D collagen network of the luminal side of the CEA strips before mechanical tests (intact state), by means of collecting Second Harmonic Generation (MPM-SHG) signals in the form of stacks of planar images.

The SHG signals detected are very specific for collagen and therefore, samples do not need to undergo any kind of manipulation nor fluorophore deployment, as required with other techniques [31][32]. Furthermore, MPM-SHG supposes an upgrade with respect to other widespread techniques, such as histology or scanning electron microscopy, as it permits a non-invasive imaging.

2.5.1. Procedure

Following tissue preparation, the strips were prepared to be imaged under the microscope, a LEICA TCS SP5 II (Germany) equipped with a Coherent Chameleon Ultra multiphoton laser (710-1040 nm)(USA) and a 20x APO water immersion objective. The system was operated through the software Leica LAS-AF.

The preparation consisted of fixing the tissue strips to translucid blocks of silicone rubber (Elastosil E41) that were fixed inside a petri dish of 10 cm, as shown in Fig. 2.5. The strips were fixed to a block in each end by neddles, leaving in between the central region that would be the gauge length in the tensile test. The luminal side of the samples was facing upwards to be imaged by the microscope. These were imaged while submerged in PBS in the petri dish (Fig. 2.5).

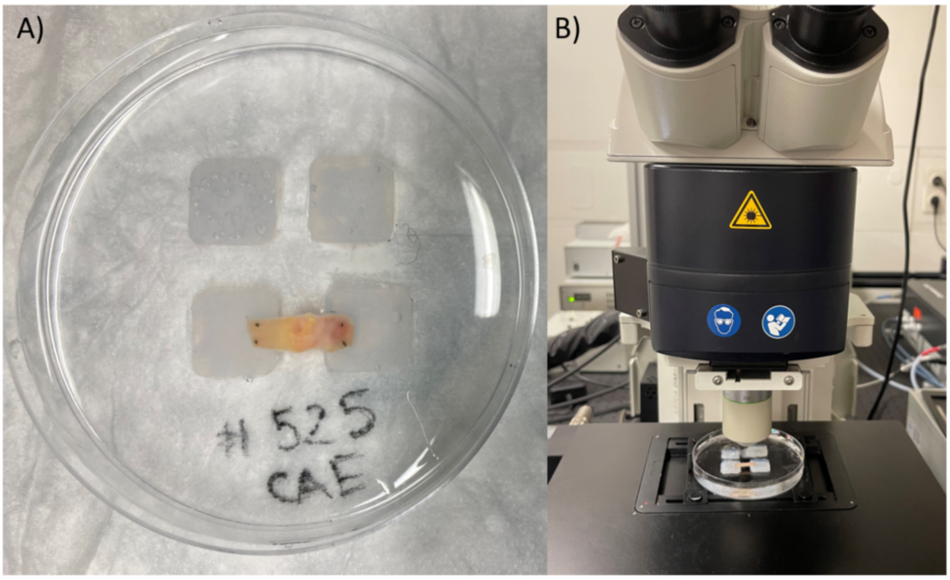

Figure 2.5: A) CEA strip fixed in two silicone blocks through needles inside a petri dish. Luminal side up. B) Petri dish filled with PBS in the Multiphoton microscope set-up.

Each strip was first imaged on the microscope using the standard bright-field mode (transmission of light). An overview image of the strip was taken as a merging of tiles (Fig. 2.6). Each tile had a size of 739 x 739 µm, and it was taken with a resolution of 5.5 µm/pixel. This low resolution permitted a quick capture of the whole strip (between 1 and 2 minutes depending on the size of the sample). A map of tiles with the coordinates of the platform positioning, was generated in the software. It allowed to know the exact location of every point in the tissue, and therefore, to place the objective in the areas intended to be imaged with SHG.

Afterward, the multiphoton laser was turned on at an excitation wavelength of 880 nm. The SHG signals from the collagen network were collected employing a non-descanned detector set at a range of 430 - 450 nm. Several tile scan elements, namely fields of view (FOVs), of 739 x 739 µm were imaged from every strip (an average ± SD of 17 ± 6 FOV/strip). They were separated between them by one FOV circumferentially and longitudinally (Fig. 2.6), with exceptions in some specimens. In each of the FOVs, a stack of axial-circumferential (in-plane) images were taken, commencing from the luminal surface and moving downward with a step size of 3.01 µm. The images had a resolution of 1.44 µm/pixel and were captured with a line average of 2 (every image twice and the result was the average). The imaging depth range of a FOV changed at every position, as it depended on the topography of the sample: it ranged from 150 to 800 µm. However, the SHG signal could only be detected up to 150 µm deep in the tissue.

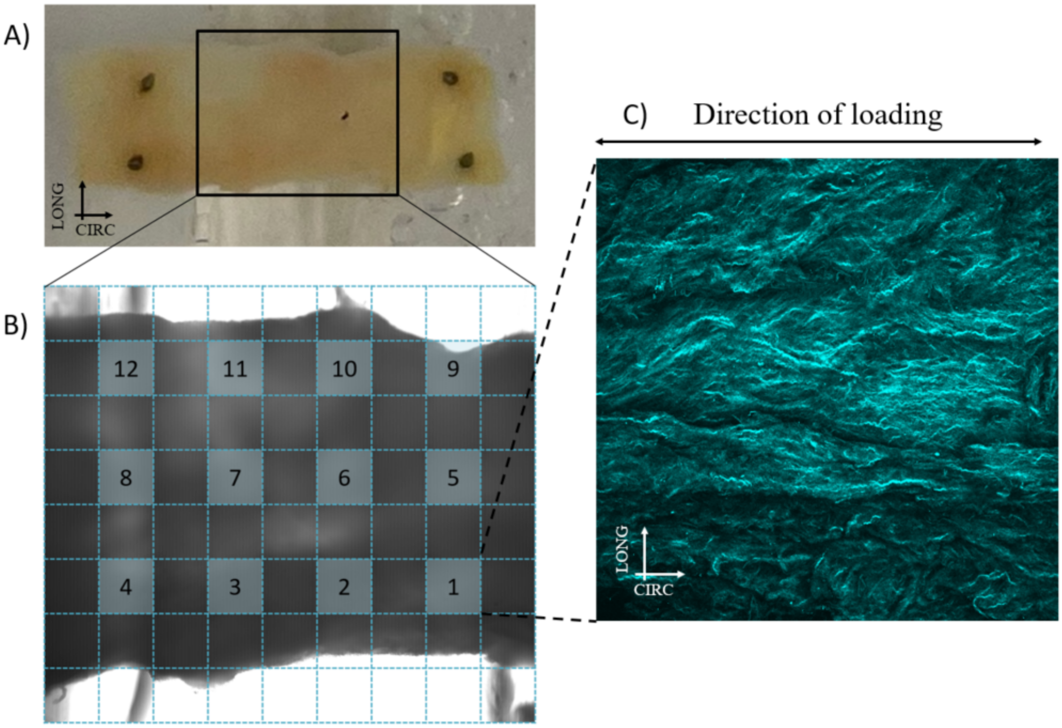

Figure 2.6: Imaging of a CEA strip under the MPM. A) Region of interest of the strip B) Tile scan overview under the microscope taken with the bright-field mode. The squares with numbers represent the different fields of view (FOVs) that are imaged with SHG signals. C) FOV maximum intensity projection composite of collagen signals in cyan.

2.5.2. Collagen structural analysis

From the stacks of images captured at the FOVs through MPM-SHG, structural parameters describing collagen fiber microstructure were extracted. The procedure is illustrated in Fig 2.7.

The images were first processed in ImageJ (NIH, USA), where maximum intensity projections (MIPs) from each FOV were obtained for subsequent analysis (A in 2.7). MIPs are planar images displaying the pixels with the highest intensity in each position throughout the whole stack of images.

Afterward, MIPs were analyzed with the FOA (Fibre Orientation Analysis) tool (S. Mariën, TU/e, Netherlands.), a program developed in Matlab that detects fibers by analysing the local tissue structure on multiple scales, based on the local Hessian matrix. Therefore, the analysis was performed regarding in-plane structure, and not out-of-plane (radial or z-direction). Fiber-like structures are found by means of the Frangi Vesselness, resulting in a probability of a pixel containing a fibre. Employing this tool, highly probable fibers were extracted using scales of [2 4 6] and vesselness thresholds of 0.999, 0.9995 or 0.9999 (B in Fig 2.7), whose performance depended on the morphology of the fibers of each image and its brightness (also with respect to noise). The eigenvector decomposition of the Hessian matrix gives the principal direction of each pixel containing a fibre. Angle distribution histograms of the found fiber orientations were derived from this tool (C in Fig. 2.7), where the zero degrees axis corresponds to the circumferential direction of the arteries (loading direction in mechanical tests).

The fiber angle histograms were later processed on Fiblab (TU/e, Netherlands), an open-source Matlab program that fits a Gaussian distribution to the histogram data, excluding a baseline that represents the isotropic fraction (P_{iso}). This program rendered for each FOV the following structural parameters (D and E in Fig. 2.7): the predominant fiber angle (μ_p), which is the angle of the highest number of fibers, the standard deviation (σ_p) of the fiber angle distribution, and the anisotropic fraction ($P_{ani} = 1 - P_{iso}$), which represents the proportion of angles that fall within the peak of the distribution [33]. P_{ani} ranges from 0 - totally isotropic to 1 – totally anisotropic.

μ_p was reported from 0° to ± 90° being the circumferential and longitudinal directions, respectively. In addition, the fiber angle difference with respect to the circumferential direction (μ_{pcirc}) was calculated to perform further analysis (0 to +90°). Both σ_p and P_{ani}, describe the dispersion of fibers. Consequently, a dispersion index (DI) comprising both parameters was defined as follows, in the form of a weighted sum:

$$DI = \frac{\sigma_p}{\sigma_{max}} * 0.5 + P_{iso} * 0.5 \tag{2.1}$$

Where σ_{max} is the standard deviation of an flat histogram (from 0° to 180°), which is equal 53. DI ranges from 0 – totally aligned fibers, to 1 – totally dispersed fibers.

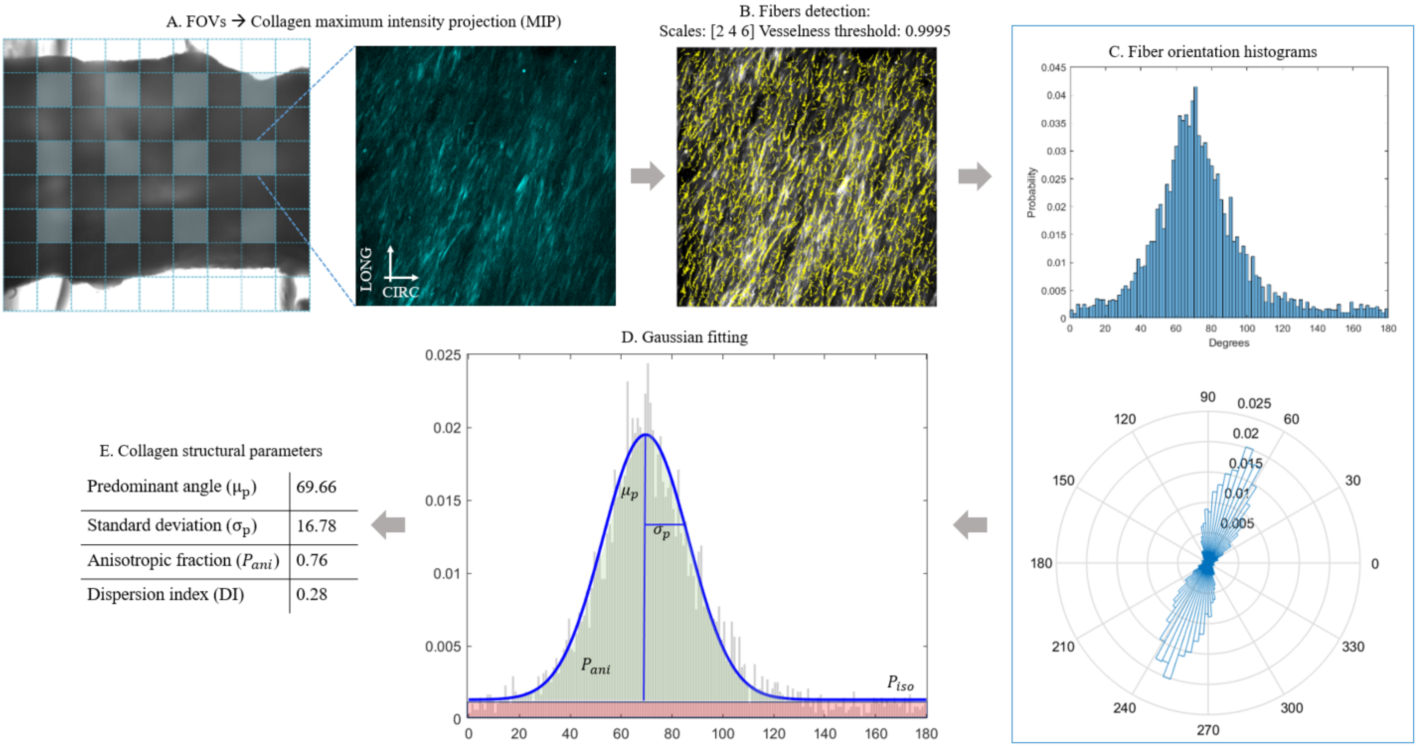

Predominant angle (μ_p)	69.66
Standard deviation (σ_p)	16.78
Anisotropic fraction (P_{ani})	0.76
Dispersion index (DI)	0.28

Figure 2.7: Procedure for the extraction of each FOV's collagen structural parameters

The values of the parameters described above were averaged for each test strip in order to relate the gross collagen organization to the global mechanical characteristics described in the next section (2.6). For the mean predominant fiber angle calculations, a Matlab Toolbox for circular statistics was employed: CircStats [34].

Finally, in order to perform visual assessments of the collagen fiber orientation and dispersion measurements within each specimen, interpolation maps showing the structural parameters for each tile of the strips were generated (Fig. 2.8). In these maps, the parameters of the areas which had not been captured, were computed through linear interpolation in Matlab (see ‘scatteredInterpolant’ function) from the measured FOVs’ parameters. Predominant fiber angles were represented by oriented lines (solid or dashed for measured or interpolated areas, respectively), and σ_p, P_{ani} and DI by color maps.

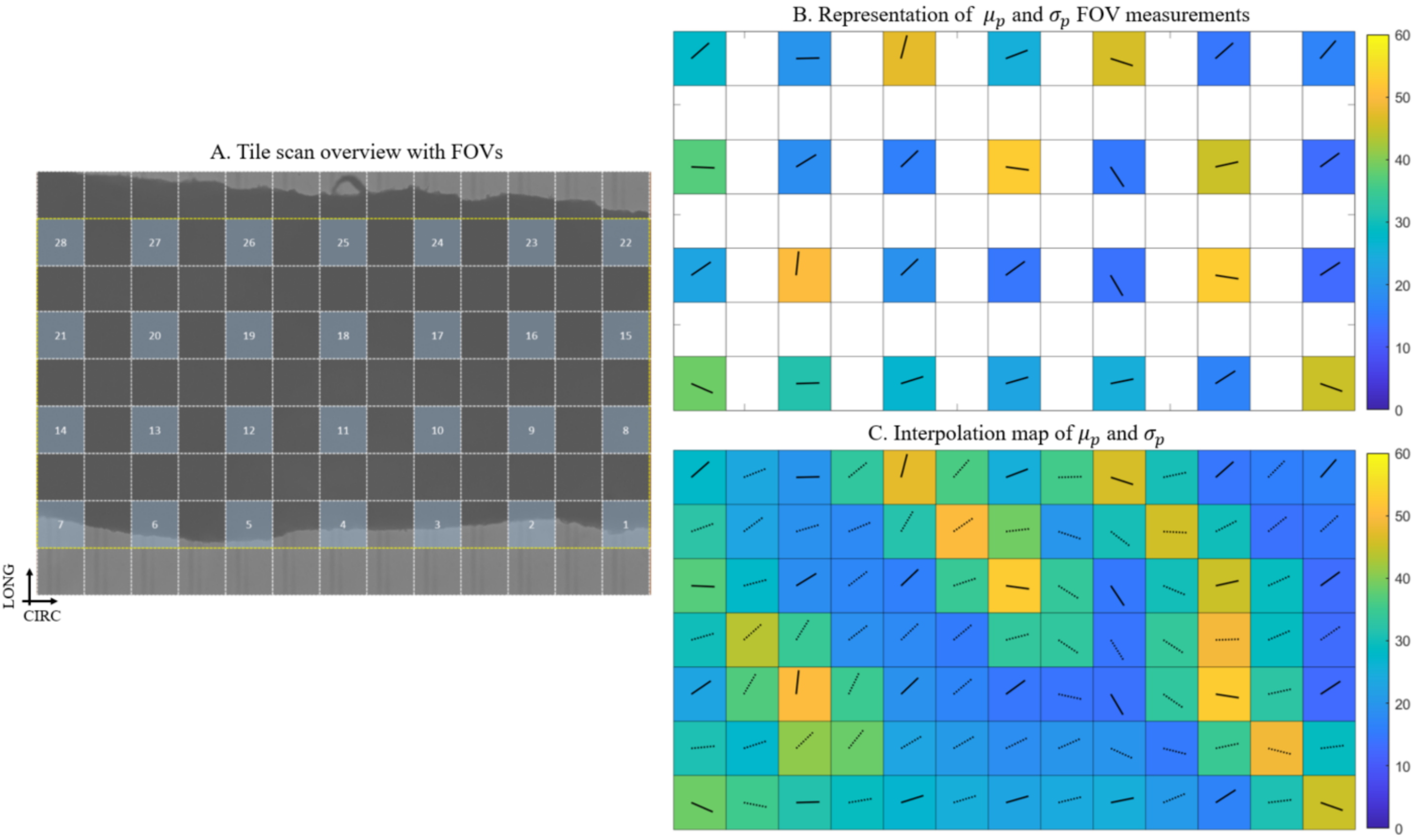

Figure 2.8: Generation of Interpolation map of predominant fiber angle (lines) and σ_p (color). A) Tile scan overview of CEA strip under MPM-SHG. FOVs indicated with numbers. B) Representation of collagen parameters from captured FOVs. C) Interpolation map created from B). Solid lines symbolize measured FOVs while dashed lines represent interpolated regions.

2.6. Mechanical testing: Uniaxial tensile tests

Uniaxial tensile tests were carried out on 31 non-calcified CEA strips after μCT and MPM-SHG imaging, to study their mechanical response to large deformation and the rupture properties in the circumferential direction. Ultrasound imaging was performed during the process to determine the thickness of the strips.

2.6.1. Experimental set-up

An in-house designed tensile tester (Fig. 2.9) mainly consisting of a cylindrical linear actuator (EACM2E10AZAK, Oriental Motor Ltd., Japan), and a 10 N load cell (LCMFD-10N, Omega Engineering Inc., USA) was employed to perform the mechanical tests. Two PVC in-house-designed clamps were used to hold the tissues. To prevent the slippage of the strips during loading, foam tape covered with sandpaper was adhered to the clamp surfaces. The performance and synchronization of the set-up was controlled by a DAQ system (LabJack U6 Pro, LabJack Corp., USA) through a custom-made script in LabVIEW (LabVIEW 2018, National Instruments Corp., USA). A scientific digital camera (PL-D725, Pixelink-Navitar

Inc., USA) with a resolution of 5.2 MP and a frame rate set at 5 fps, was placed on top of the set-up to obtain video recordings of the tissue deformation during the tensile tests, for further DIC analysis (Section 3.3.1). A lens of 50 mm focal length (MVL50M1, Thorlabs Inc., USA) was mounted on the camera through a 10 mm extension ring. A ring light source was located below the camera to lighten the field of view and acquire clear images of the tissue surface. In order to mimic body temperature (37 °C) [35] and keep the tissues hydrated during the tests, an in-house made heating bath was incorporated in the set-up and filled with PBS.

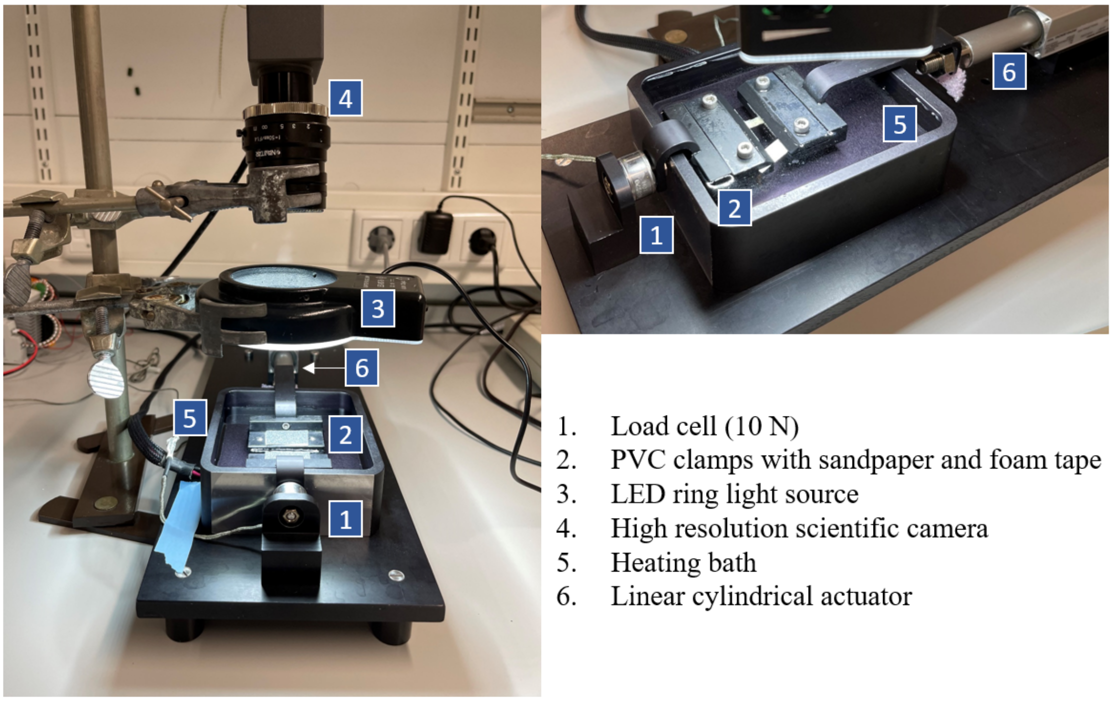

1. Load cell (10 N)
2. PVC clamps with sandpaper and foam tape
3. LED ring light source
4. High resolution scientific camera
5. Heating bath
6. Linear cylindrical actuator

Figure 2.9: Custom designed uniaxial tensile tester with the different parts indicated. Image in the right shows a CEA strip prepared for testing.

2.6.2. Test procedure

Before the mechanical tests, an airbrush gun was employed to spray black tissue marking dye (Boekel scientific, USA) on the luminal surface of the specimens, in order to generate a suitable speckle pattern for the posterior DIC analysis (Fig. 2.10). For an optimal DIC performance, the region of interest (gauge length) of the samples may had a random, uniform and high contrast speckle pattern, aiming to make each area of the surface univocally identifiable. In addition, the size of the speckle dots had to be in accordance with the sample size and camera resolution [36]. The samples were sprayed from a distance of 40 cm approximately in short pulses, until the whole surface was covered with a consistent pattern.

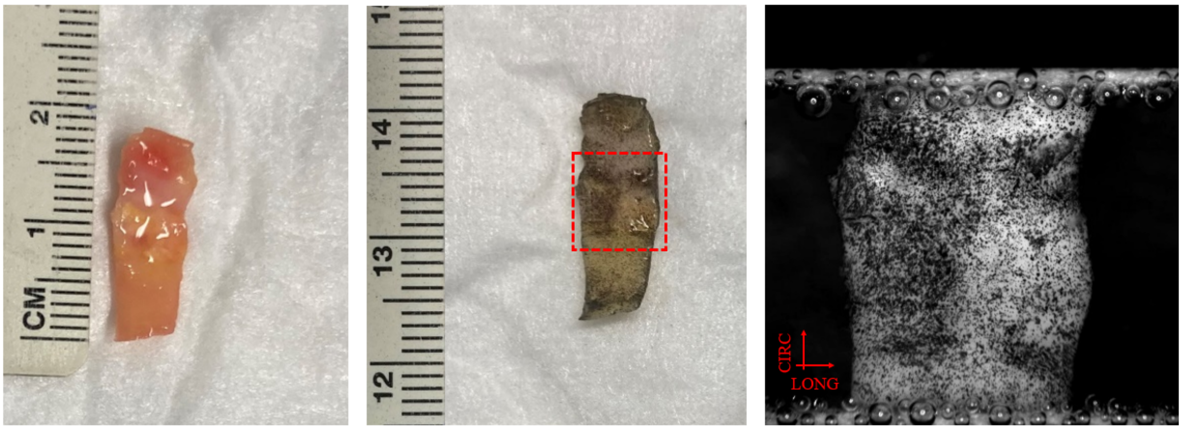

Figure 2.10: Speckle pattern generation for uniaxial tensile testing. CEA strip after excision (left), after tissue marker spray (middle)(in red gauge length region), and fixed between the clamps of the tester under the camera (right).

The strips were positioned within the clamps, leaving approximately the same length of tissue inside both grips. A torque screwdriver (Garant, Hoffman group, Germany) was employed to secure the strips inside the clamps with a uniform torque of 20 cNm, ensuring that the clamping force remained equal for all the screws without damaging the tissues. The initial gauge length (before pre-stretch) was set such that the WL ratio of the strips was less than one. The heating bath was filled with PBS until test strips were completely submerged. All the strips were visually checked to ensure the absence of tears or imperfections that could influence the tests.

Sequentially, the experiments followed the next steps:

1. Pre-stretching up to 0.05 N, to straighten the samples.
2. Preconditioning up to 10 % stretch for 10 cycles.
3. Stretching until complete failure.

The displacement speed of the movable clamp was set to 0.05 mm/s^{-1} to achieve quasi-static deformation that allowed acquiring the full characteristics of the mechanical behavior [12]. After the pre-stretch, ultrasound B-mode images of the longitudinal cross-section of the strips were taken to accurately measure the thickness of the samples in the gauge length. This was performed using a Vevo 3100 ultrasound system (VisualSonics, Canada) with an axial resolution of 75 µm, a center frequency of 21 MHz (MX250 transducer), and a frame rate of 100 fps.

In addition, images of the strips were acquired by the camera to measure their width. Later on, the width and thickness of the gauge length of the specimens at the pre-stretched state were obtained by tracing 10 equally spaced lines at the calibrated images in ImageJ (NIH, USA) and doing the average of their measurements. The stretching tests were recorded at 5 fps to perform the subsequent DIC analysis and study the rupture location and progression. The tensile tester recorded the force and actuator movement data at a sampling rate of 25 s^{-1}.

2.7. Global mechanical analysis through traditional methods

To investigate the global mechanical properties of the strips, the force-displacement curves of the tests were analyzed through a custom Matlab (r2019a, Natick, Massachusetts: the MathWorks Inc.) script. The load cell recorded the force derived during the stretching of the samples, and the displacement was based on the gauge length (GL-based) (Fig. 2.9). Subsequently, the stretch ratio (λ) and the Green-Lagrange strain (ε) values – for the latter for the comparison with DIC strain results-, were computed according to (Eq. 2.2). On the other hand, the Cauchy stress (σ) values were computed under the assumption of incompressibility of the material, which states that the volume of a material remains constant during deformation [37].

$$\lambda = \frac{L}{L_o}, \quad \varepsilon = \frac{1}{2}(\lambda^2 - 1), \quad \sigma = \lambda \frac{F}{A_o} \tag{2.2}$$

Where F represents the applied force measured by the load cell (N), A_o is the reference cross-sectional area of the sample (mm^2) at the pre-stretch state, L is the current gauge length and L_o is the reference gauge length (pre-stretch state).

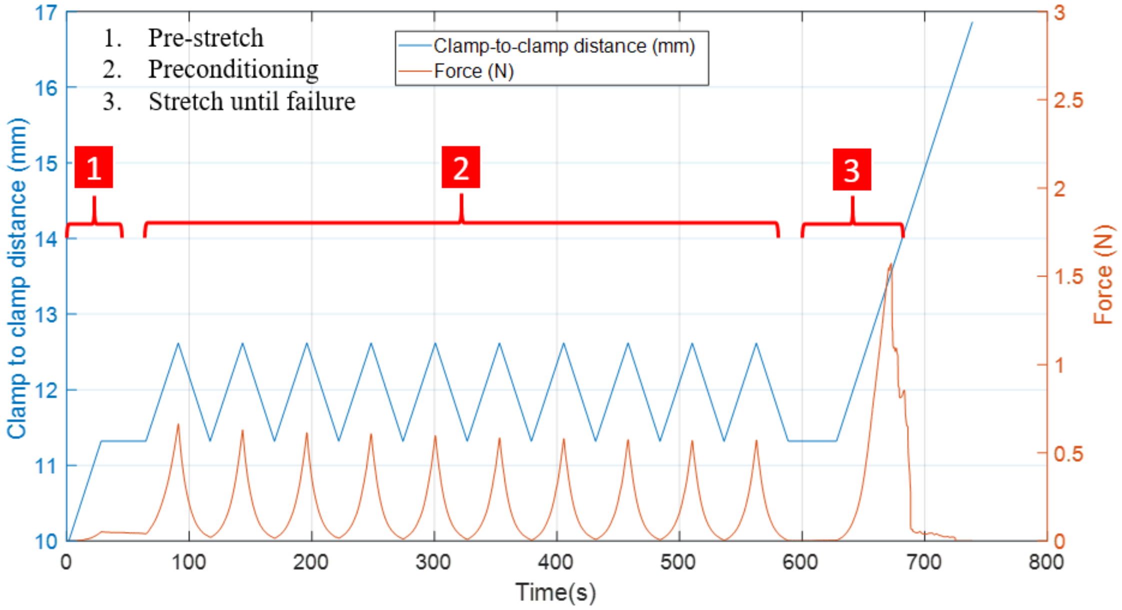

Figure 2.11: Plot of force (N) and clamp-to-clamp distance (mm) raw data vs time showing the different steps of the tensile test procedure.

Quantitative measurements of the **stiffness** of the samples were extracted in the form of **tangential modulus**, at different stretch ratio levels (every 0.025) until 0.025 stretch before tissue started to rupture. Linear regression was performed between data points ranging 0.012 stretch below and above those central points (Top panel Fig. 2.12). The tangential moduli were calculated as the slope of the fitted lines (Modified from [38]).

The **inflection** or transition point of the curve was determined as the point where the second derivative of the stress-stretch ratio curve before rupture starting was maximum, representing the maximal change of slope [39]. To compute it, an 8th degree polynomial equation was fitted to the curve until the first local maxima, and the maximum point of the second derivative of this equation was selected (Bottom panel Fig. 2.12). Experimental data was first smoothed using a centered moving average fit

(50 sampling points) to permit a good fitting (see ‘movmean’ function in Matlab documentation.

The **ultimate tensile strength (UTS)** and the associated **ultimate stretch ratio (USR)**, for studying the rupture behavior of the samples, were derived from the maximum point of stress at the stress-stretch relationships (Top panel Fig. 2.12) that preceded a sudden drop of the curve [28][40]. Samples were categorized into two groups with respect to the location of the rupture: clamp region rupture group and central region rupture group. The clamp region was defined as the areas up to 1 mm far from the grips.

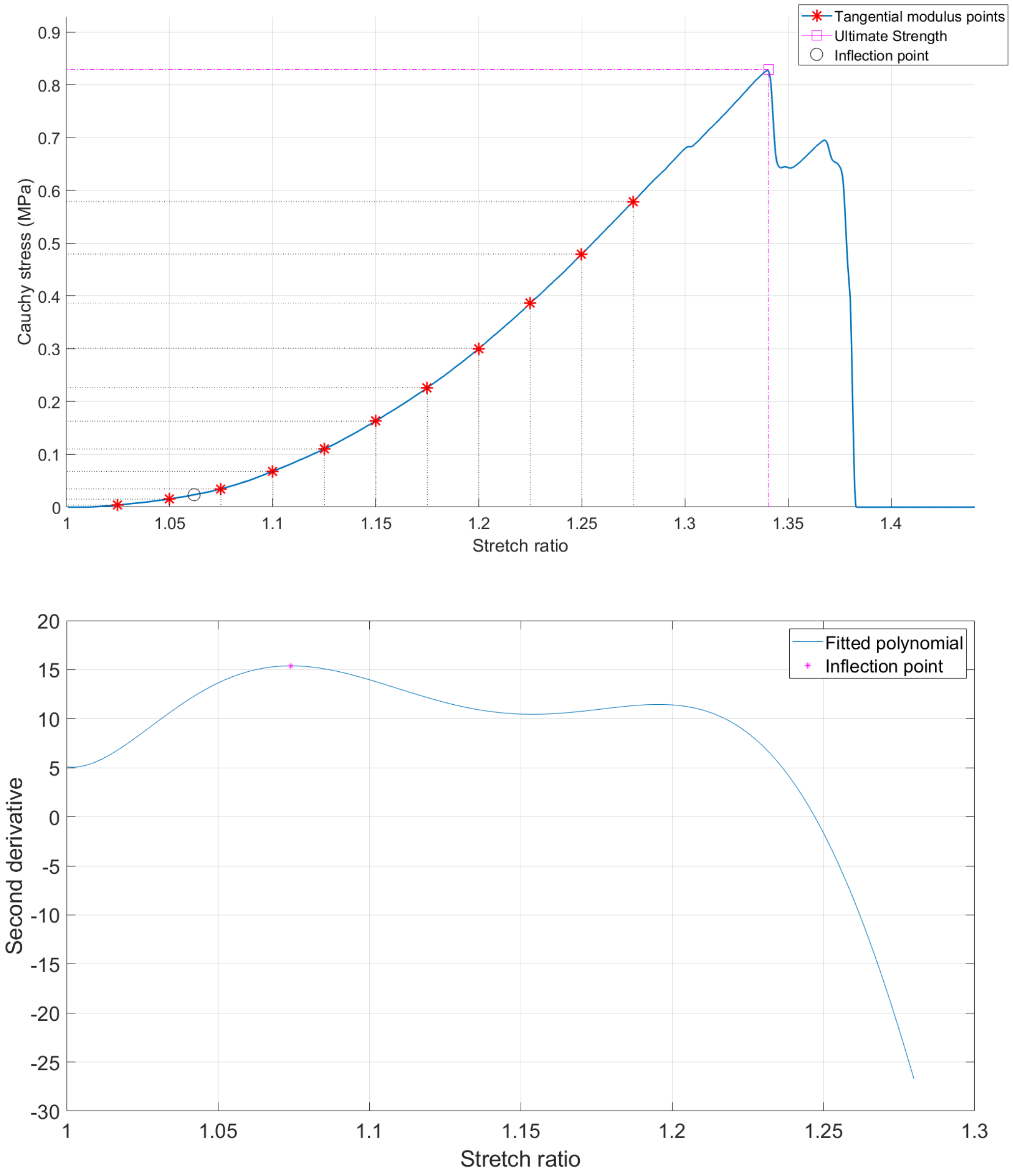

Figure 2.12: Top) Final stretching of the tissue until failure, showing the points of the analysis at the post-processing. Bottom) Second derivative of the first part of the curve, showing the maximum, which is selected as the inflection point.

2.8. Local mechanical analysis

2.8.1. Digital Image Correlation analysis

2D Digital Image Correlation (DIC) analysis was employed to study the local strains of the luminal surface while undergoing tensile deformation, focusing on rupture location and development. DIC is a contactless optical technique that measures the change of the speckle pattern on the specimens by comparing the images of the deformed states during the testing procedure to the undeformed state (reference image). The images are divided into smaller subsections (subsets) and a matching algorithm relates them to those of the reference state. The full-field displacements are computed, and eventually, the strains through derivation [36]. To the author's knowledge, this is the first time an exhaustive DIC analysis targetting strain patterns in atherosclerotic plaque tissues is carried out.

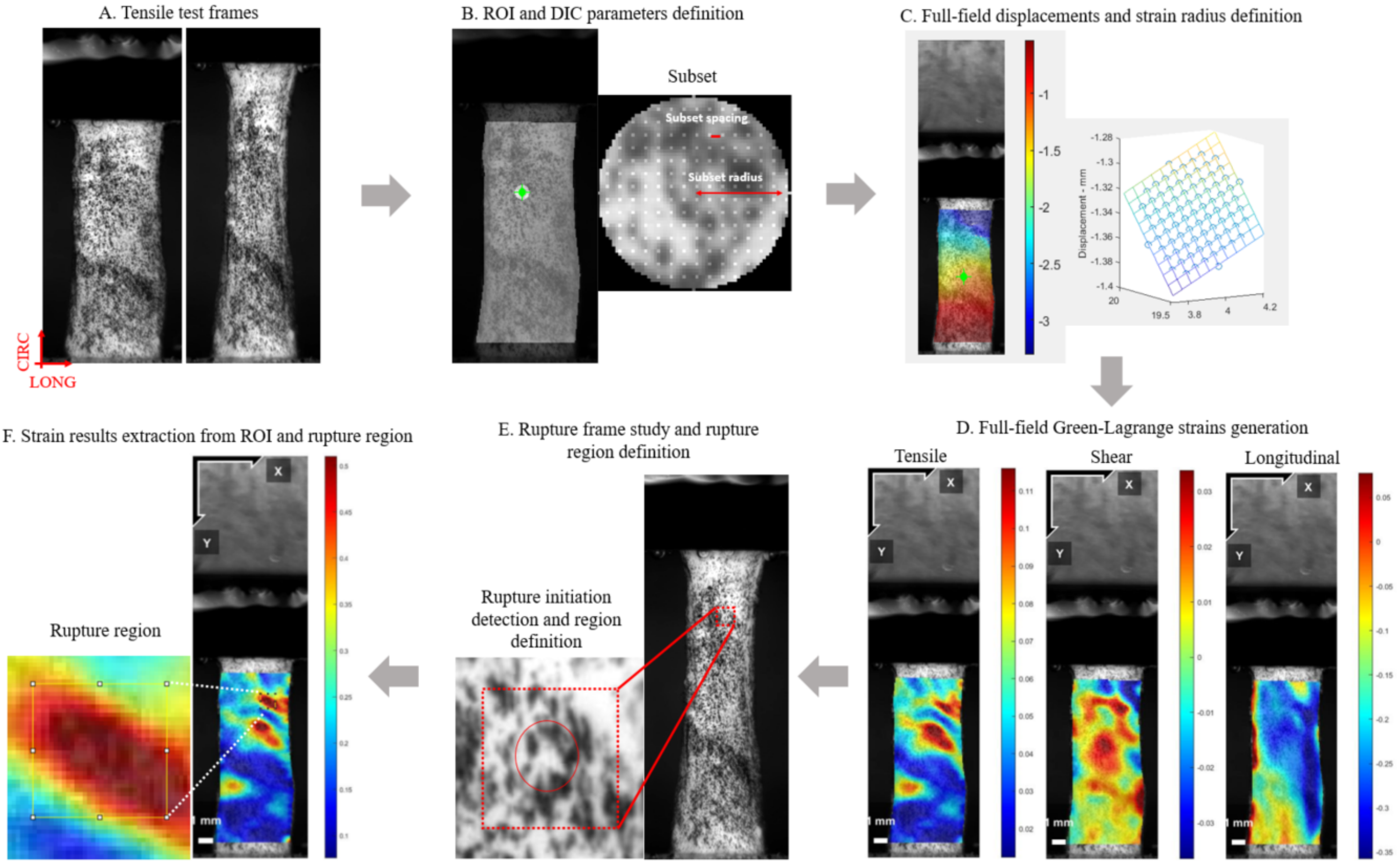

Figure 2.13: Steps of the DIC and local strain analysis

The DIC analysis was performed on the videos recorded during the tensile tests of the CEA samples through Ncorr (v1.2, [41]), an open-source 2D DIC Matlab program (A and B in Fig 2.13). For each sample, the DIC analysis was carried out employing a subset radius of 30 pixels (size of the subsets to evaluate), a subset spacing (distance between the center of the subsets) of 3 pixels, and an iteration cutoff and the norm of the difference vector cutoff of 50 and 10^{-5}, respectively (B in Fig. 2.13). Additionally, to address the large deformation of the samples, the reference image in the analysis was updated every 5 frames. Finally, Green-Lagrange strains were computed (ε_{xx} = longitudinal,ε_{xy} = shear ,ε_{yy} = tensile (or circumferential)) (D in Fig. 2.13) by setting a strain radius of 5 (number of displacement points where to fit a plane for subsequent derivation) (C in Fig. 2.13). The reference image set corresponded to the frame showing the strip after preconditioning and before undergoing the final tensile loading.

To study rupture, visual inspection was performed on the camera recordings for the first clear visible rupture at the central region of the strips. The DIC-based strains were evaluated at the frame right before rupture occurred, which was named as ‘Rupture frame’ (E in Fig 2.13). Concretely, the strains at the central region (ROI), as defined in Section 2.6 and at the rupture region, which was defined as a square of 1 x 1 mm centered at the point where rupture started (E and F in Fig. 2.13), were investigated. The analyses of ruptures occurring at the clamp region were avoided due to unreliable results.

Apart from the “Rupture frame”, the DIC-based strain results at the frame corresponding to a global deformation of 0.05 Green-Lagrange strain (from the global stress-strain curves), called as “Physiological frame”, were investigated. The purpose was to study the values and patterns of strain at a physiological stretch level and observe if rupture could be predicted from a low deformation [42].

From the DIC results, the average, standard deviation, maximum and minimum of the Green-Lagrange strains (ε_{xx},ε_{xy}, and ε_{yy}) were acquired from both the whole ROI and the rupture region at the “Rupture and Physiological frames”. The full-field strain distribution maps representing tensile, longitudinal and shear strains were visually assessed in search of characteristic strain fingerprints, specifically at the rupture region. Note that the strain maps (D and F in Fig. 2.13) are plotted on top of the reference images since they illustrate the displacement of the points of the surface with respect to the original configuration.

2.8.2. Local collagen analysis at specific strain regions

In order to relate collagen structural properties and the DIC-based strains of the strips, the local collagen structural parameters of the rupture, high and low tensile strain regions were identified for later comparisons.

To do so, the reference images of the DIC analysis (2 in Fig. 2.14) and the DIC strain distribution maps (3 in Fig. 2.14) at the “Rupture frames” were faced with the corresponding tile scan overview images taken under MPM (4 in Fig. 2.14). Apart from the rupture region (white square in Fig. 2.14), previously identified, high and low strain regions, with respect to the average ROI strain, were localized at the DIC results (red and blue squares in Fig. 2.14). Subsequently, these same regions were located at the tile scan overview. The MPM-SHG fields of view that were closer to the regions were selected as the corresponding areas and their collagen structural parameters retrieved. This identification in the tile scan overview was carried out by following the characteristic outline of each strip while knowing the scales of the images.

Collagen structural parameters were averaged for all samples and compared between the three different regions (Rupture, high and low strain). High strain regions did not include ruptured regions to investigate why those did not fail.

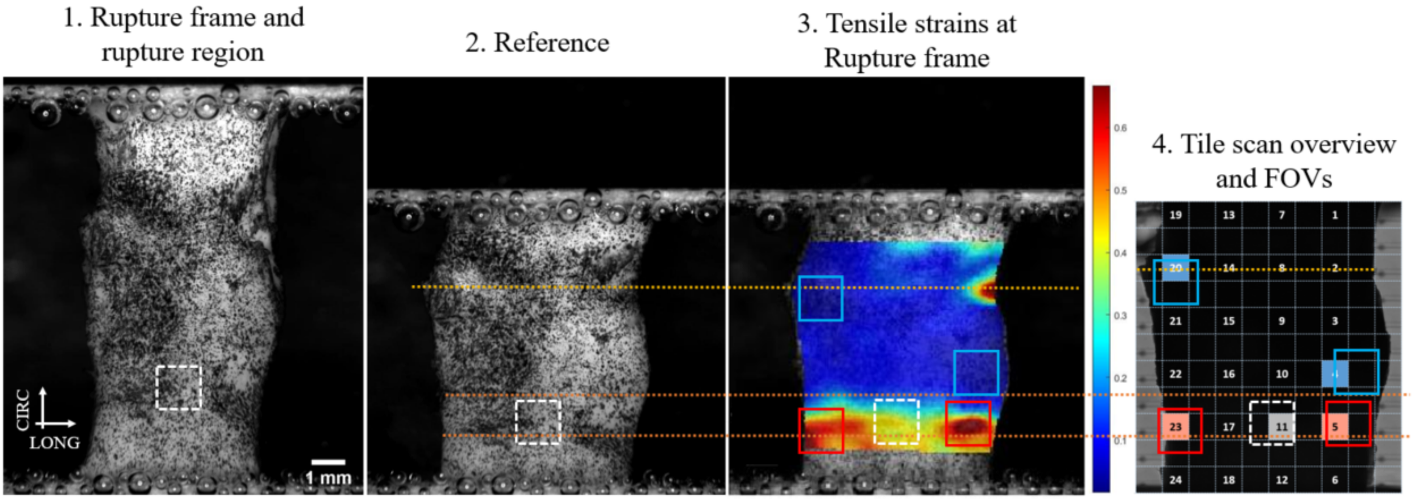

Figure 2.14: Representative strip showing the steps for identifying rupture (white square), high and low (red and blue squares) tensile strain regions at the Tile scan image under MPM-SHG. The collagen structural parameters at the corresponding fields of view were retrieved (Rupture: FOV 11, high strain: FOVs 23 and 5, low strain: FOVs 20 and 4).

2.9. Statistical analysis

All variables were evaluated for normality using the Shapiro-Wilk test. For normally distributed variables, data are reported through mean and standard deviation. Non-normality distributed variables are reported in terms of the median and range.

Two-sample T-tests were performed to assess the differences of mechanical and structural parameters between grouped datasets. Significant relationships were evaluated using Spearman’s (ρ) correlation tests.

Statistical significance was assumed if $p<0.05$. All statistics were performed in Matlab.

3

Results

In this section, the MPM-SHG-based collagen structural properties of the CEA samples, and their global and local mechanical properties under uniaxial tensile tests, acquired through traditional methods (gauge length-based) and DIC analysis, are presented.

3.1. Collagen structural properties

The intact CEA strips (n=31) were successfully imaged by using the MPM-SHG. The majority of the FOVs imaged displayed a clear collagen network, while only a few exhibited collagen poor areas (505 vs 27 FOVs), which were not analyzed.

A representative case (Sample 534-1) is illustrated in Fig. 3.1. Some collagen MIPs from the imaged FOVs are displayed, along with the extracted collagen structural parameters: the predominant fiber angle (μ_p), the standard deviation (σ_p) and the anisotropic fraction (P_{ani}), of the Gaussian fitted distributions, and the dispersion index (DI). A large intra-sample variation regarding these parameters can be noticed for this representative case (average ± SD of μ_p: 17.54° ± 36.85°; σ_p: 26.05° ± 7.27°; P_{ani}: 0.45 ± 0.18; DI: 0.53 ± 0.1). The interpolation map included illustrates this heterogeneity. Several interpolation maps exhibiting the collagen organization of other strips are included in the Appendix 6.0.3.

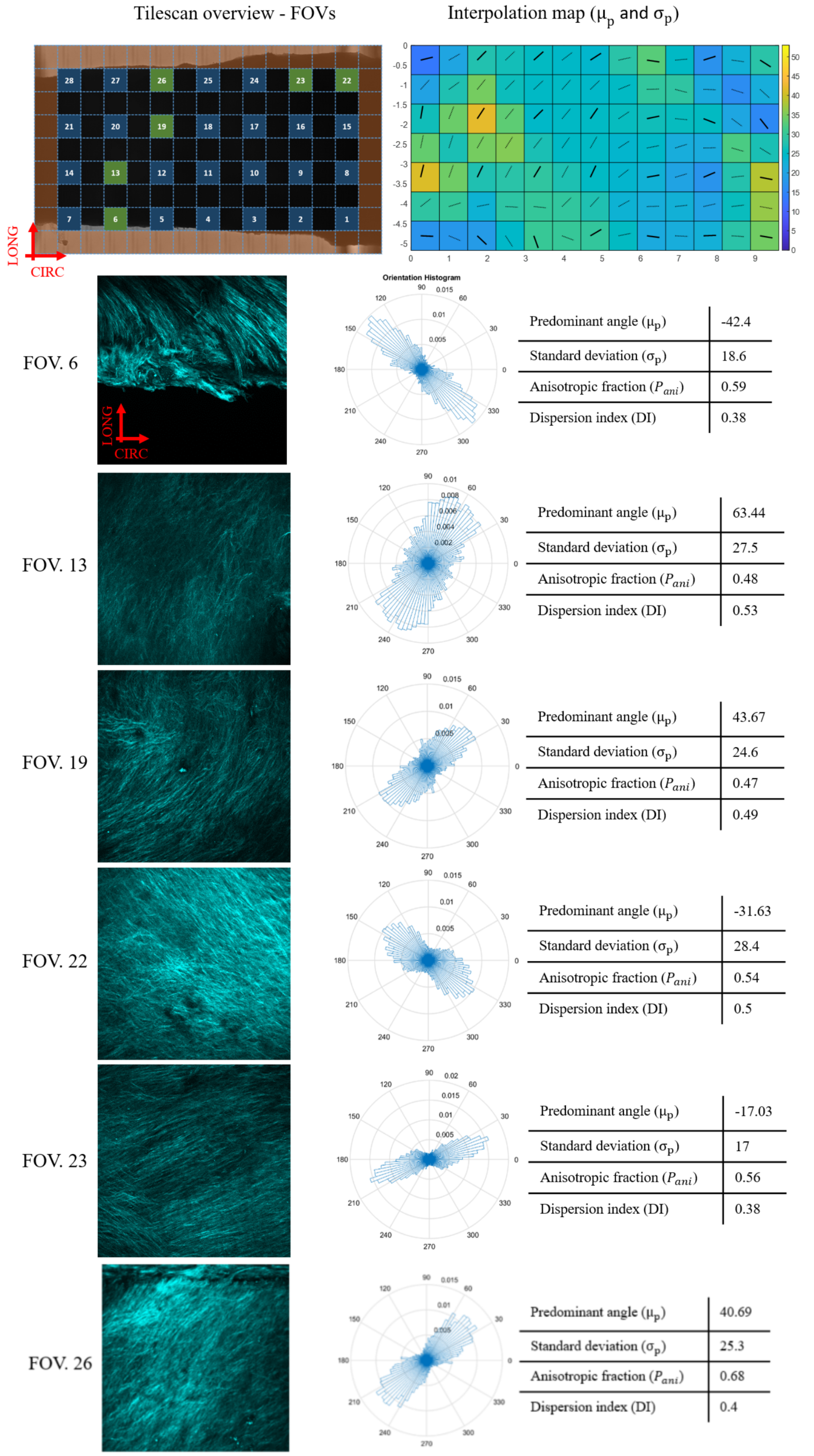

FOV. 6

Predominant angle (μ_p)	-42.4
Standard deviation (σ_p)	18.6
Anisotropic fraction (P_{ani})	0.59
Dispersion index (DI)	0.38

FOV. 13

Predominant angle (μ_p)	63.44
Standard deviation (σ_p)	27.5
Anisotropic fraction (P_{ani})	0.48
Dispersion index (DI)	0.53

FOV. 19

Predominant angle (μ_p)	43.67
Standard deviation (σ_p)	24.6
Anisotropic fraction (P_{ani})	0.47
Dispersion index (DI)	0.49

FOV. 22

Predominant angle (μ_p)	-31.63
Standard deviation (σ_p)	28.4
Anisotropic fraction (P_{ani})	0.54
Dispersion index (DI)	0.5

FOV. 23

Predominant angle (μ_p)	-17.03
Standard deviation (σ_p)	17
Anisotropic fraction (P_{ani})	0.56
Dispersion index (DI)	0.38

FOV. 26

Predominant angle (μ_p)	40.69
Standard deviation (σ_p)	25.3
Anisotropic fraction (P_{ani})	0.68
Dispersion index (DI)	0.4

Figure 3.1: MPM-SHG images and collagen structural parameters from sample 534-1. Top left: Tile scan overview with all FOV captured (in green: the FOVs displayed below). Top right: Interpolation map showing μ_p (solid lines: FOVs captured, dashed lines: interpolated) and σ_p (color map). Below: MIPs from different FOVs, with the corresponding orientation histograms and the structural parameters extracted.

The distribution of the FOV predominant fiber orientations (μ_p) for all samples are demonstrated in Fig. 3.2. The majority of the μ_p measurements were between -45° and +45° (in 439 out of 505 FOVs). Only three strips showed the majority of their μ_p measurements outside this range (527-1, 529-1, 539-1). These results indicate that the collagen fibers in the samples were oriented closer to the circumferential direction of the artery than the longitudinal direction. The standard deviations plotted in Fig. 3.2 demonstrate the high intra-sample variation of the predominant angle (average: 21.5°). These observations are further supported in Fig. 3.3, where the predominant fiber angle difference from the circumferential direction (μ_{pcirc}) of the FOVs per strip is displayed. For the whole sample set, the average ± SD of μ_p was 20.8° ± 10.5°, which suggests also a certain inter-sample variability in collagen fiber orientations.

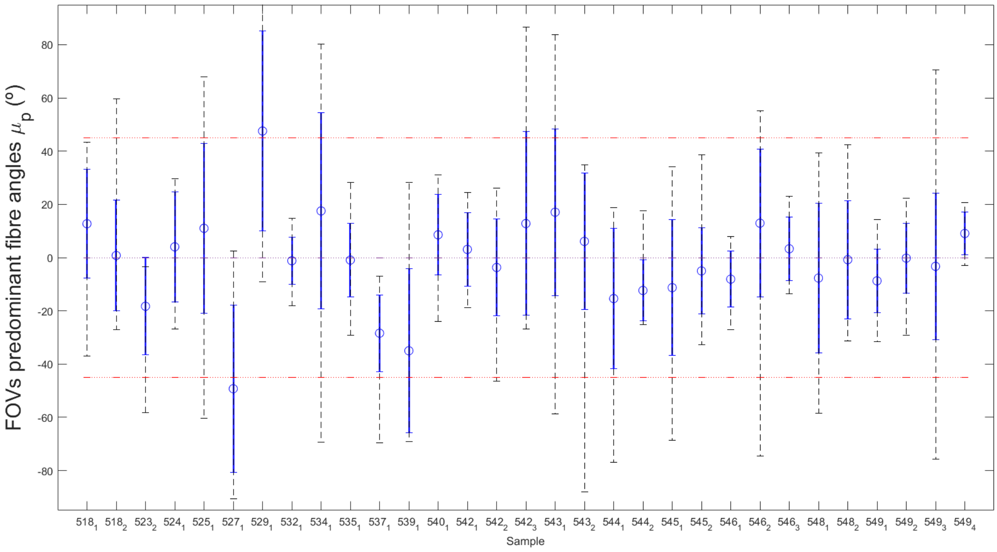

Figure 3.2: FOVs predominant fiber angles μ_p (°) distribution per sample. The circle indicates the mean, the blue solid bar the SD, and the black dashed bar the range. Zero degree corresponds to the arterial circumferential direction.

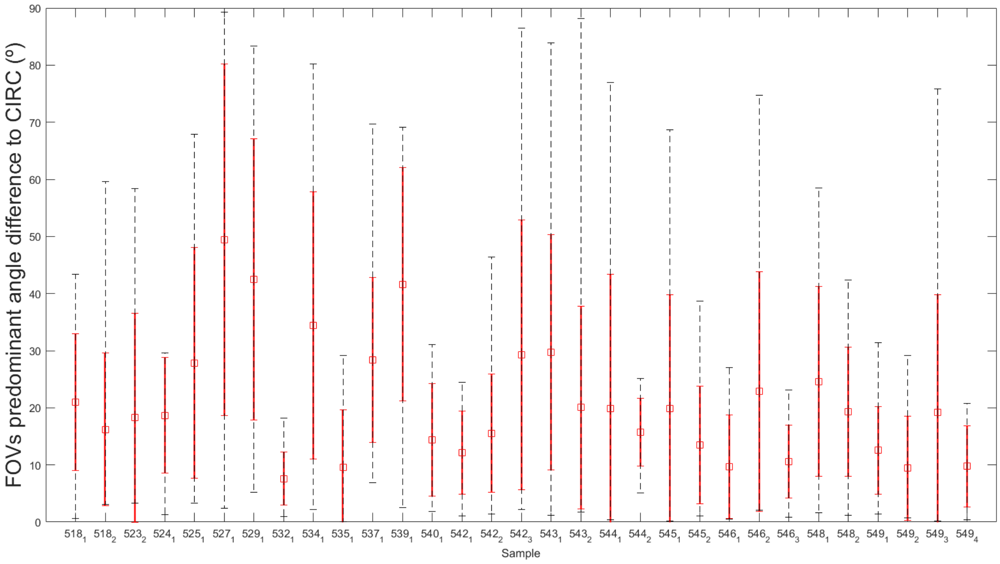

Figure 3.3: FOVs predominant fiber angle difference from the circumferential direction μ_{pcirc} per sample. The square indicates the mean, the solid red bar the standard deviations and the dashed black bar the ranges. Degrees from 0° (circumferential) to +90° (longitudinal).

Regarding the dispersion of the fibers, Fig. 3.4, 3.5 and 3.6 display an overview of σ_p, P_{ani}, and DI, respectively, for all samples. The mean ± SD of the average of these three parameters per strip for the entire sample set were 24.8° ± 3.1°, 0.48 ± 0.1 and 0.50 ± 0.06, respectively. From these values, it was inferred that generally, the collagen fibers within a FOV do not have a perfect parallel alignment in the predominant fiber direction, but have a certain level of dispersion. The standard deviations of these measurements revealed that the intra-sample variation was similar for all the strips.

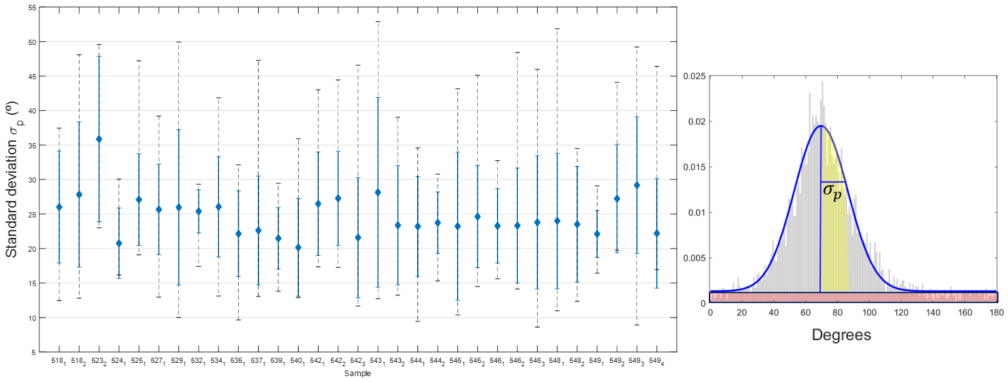

Figure 3.4: FOVs standard deviations (σ_p) per samples, obtained from the Gaussian distribution fitted at the fiber angle histograms (right). The diamond indicates the mean, the solid blue bar the standard deviation and the dashed black bar the range.

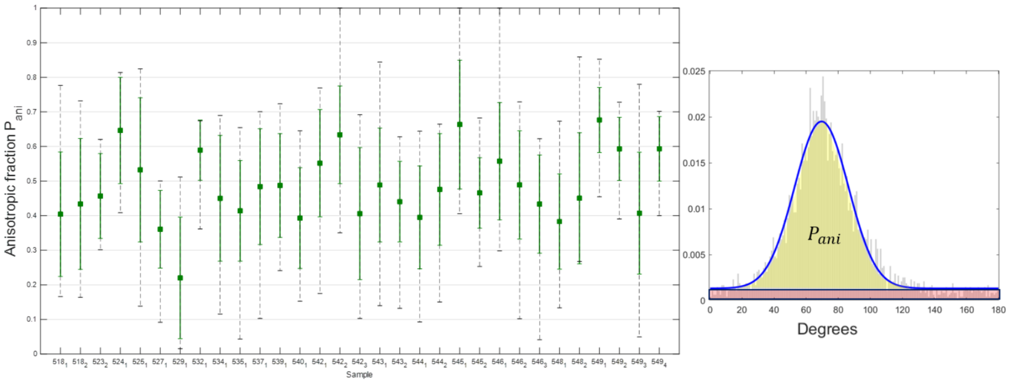

Figure 3.5: FOVs anisotropic fractions (P_{ani}) per samples, obtained from the Gaussian distribution fitted at the fiber angle histograms (right). The square indicates the mean, the solid green bar the standard deviation and the dashed black bar the range.

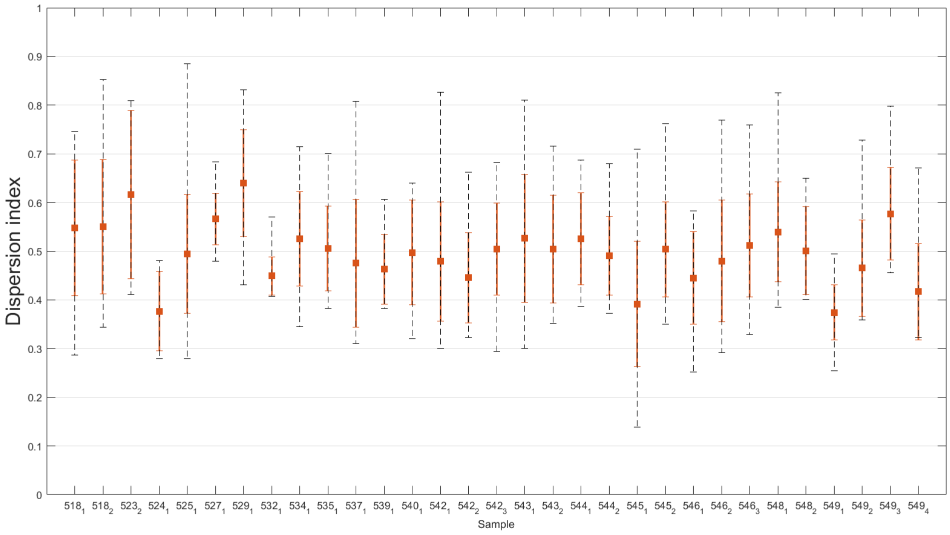

Figure 3.6: FOVs dispersion indices (DI) per sample. The square indicates the mean, the solid orange bar the standard deviation and the dashed black bar the range.

Interestingly, a significant negative linear correlation was found between the predominant angle difference from the circumferential direction and the anisotropic fraction for all the FOVs analyzed (n=505) (Spearman's ρ = -0.27, p-value = <0.001), indicating that the more circumferential the predominant direction of the fibers are, the less dispersed those fibers are (Fig. 3.7).

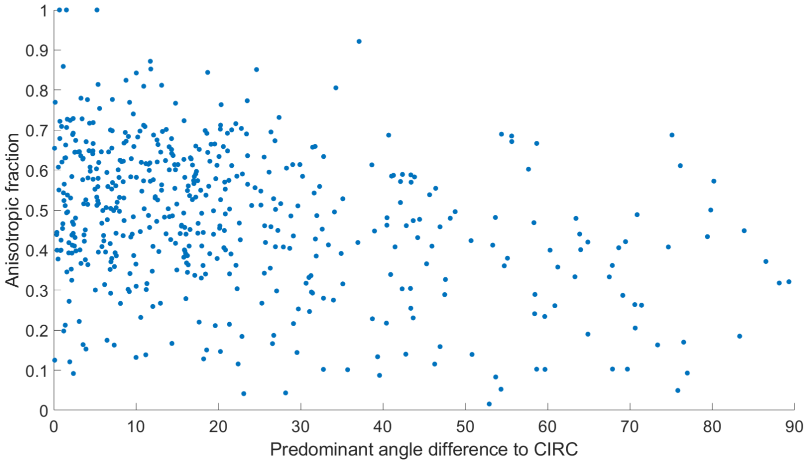

Figure 3.7: Anisotropic fraction versus Predominant angle difference to the circumferential direction of all the FOVs analyzed.

3.2. Global mechanical properties

The global mechanical results obtained through traditional gauge length-based methods are described in this section, along with correlations with the global collagen structural parameters of the samples obtained from the MPM-SHG images. All non-calcified CEA (n=31) tissue strips were tested under uniaxial tensile tests in the circumferential direction until rupture. Two of them were excluded from the subsequent analysis due to slippage and load cell measurement errors. The Cauchy stress-stretch ratio relationships for all the 29 specimens analyzed until ultimate rupture are shown in Fig. 3.8. The mechanical response of the CEA samples was non-linear, presenting the typical J-curve at the initial region, also typical for healthy vascular tissue, which was followed by a decrease in stiffness at larger deformations.

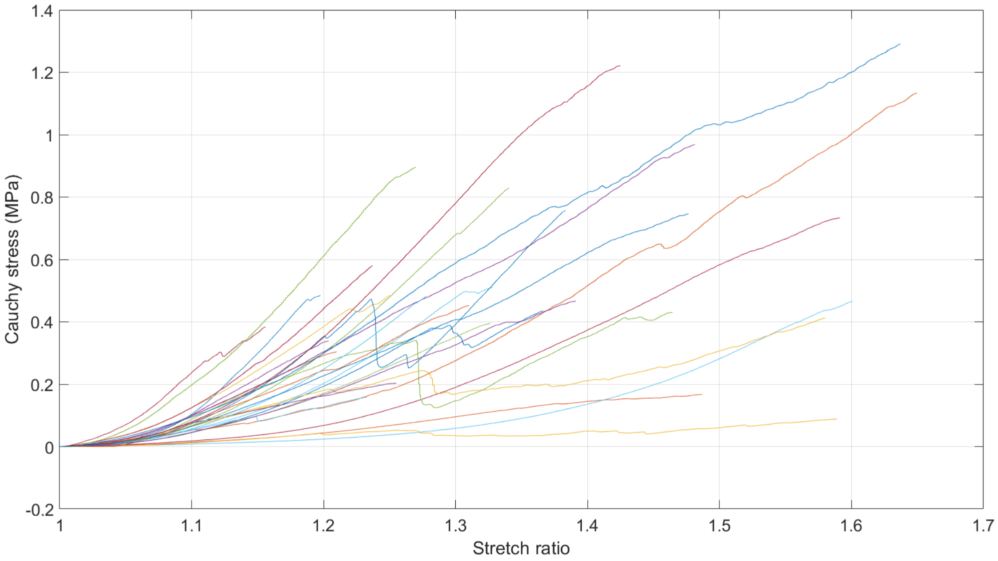

Figure 3.8: Cauchy stress vs stretch ratio curves for all the non-calcified CEA strips analyzed (n=29) until ultimate rupture.

3.2.1. Pre-failure

Regarding the stiffness, the tangential moduli at different stretch levels are presented in Fig. 3.9, showing a high inter-sample variability. It was observed that stiffness increased with deformation. However, the increasing rate was seen to lessen with large deformations. Note that not all the tangential moduli were calculated until the same level, since strips started to rupture at different stretch levels. The average stiffness values ranged from 0.43 (at 1.025 stretch) to 2.24 (at 1.325 stretch) MPa. The average tangential modulus of the samples at a stretch ratio of 1.075, which counts with the contribution of all the specimens (n=29), is 1.15 ± 0.77 MPa. Besides, the average last tangential modulus (stiffness for larger deformation) calculated for all strips is 2.23 ± 1.22 MPa.

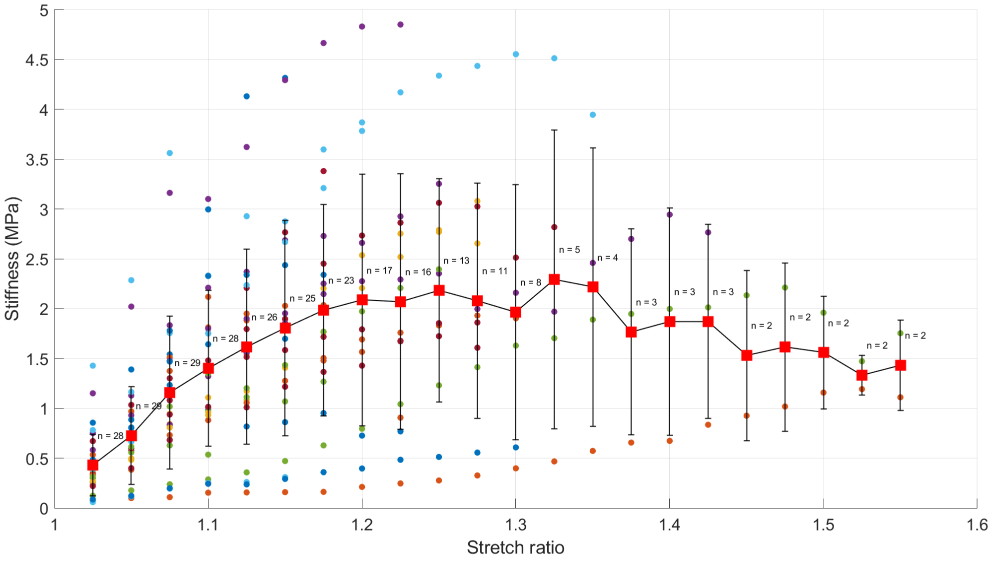

Figure 3.9: Tangential moduli of all the strips (filled circles, each strip a different color), with the average (red squares) and standard deviation (black vertical bars) calculated at the different stretch ratio levels. The sample size at every level is indicated at the right of each bar.

On the other hand, the inflection points calculated represented the maximum slope change of the stress-stretch curves. The strip that underwent slippage was also included in this measurement (548-1), since the slippage occurred at large deformation after the inflection point. Stress and stretch datasets of the inflection points were not normally distributed according to Shapiro-Wilk tests. The median values of Cauchy stress and stretch ratio for all the inflection points are 0.03 MPa and 1.07, with ranges of 0.21 MPa and 0.43, respectively. These points can be seen plotted in the Appendix 6.0.1.

3.2.2. Failure

It was observed that 21 strips ruptured at the clamp region while the other 8 ruptured at the central region. The average ± SD of the (Cauchy) ultimate tensile strength (UTS) of the samples that ruptured at the center and at the clamp are 0.40 ± 0.11 MPa and 0.61 ± 0.36 MPa, respectively. The corresponding average ± SD of the ultimate stretch ratio (USR) of the two groups are 1.29 ± 0.11 and 1.41 ± 0.16, respectively (Fig. 3.10). Statistical analysis showed no significant differences between ultimate values of the two groups. The average ± SD of the UTS and USR for all strips combined were 0.55 ± 0.32 MPa and 1.38 ± 0.15, respectively (Fig. 3.10). The dimensions, locations of rupture and ultimate parameters of the successfully tested strips are included in the Appendix 6.0.2.

To study the impact of the test sample dimensions on the rupture location (central vs.clamp region), the WL ratios, initial gauge lengths and initial widths were compared between the two groups (Fig. 3.10). The samples that ruptured at the central region had an average ± SD of the WL ratio of 0.49 ± 0.15 whereas the clamp region rupture strips had an average ± SD of 0.67 ± 0.16. The two-sample t-test reported significant differences (p-value=0.012). The central rupture samples also had statistically significantly greater initial gauge lengths than the clamp region rupture strips (8.21 ± 2.66 vs. 5.38 ± 1.96, p-value=0.003) but not for the initial width of the strips (central rupture: 3.84 ± 1.14 vs clamp rupture: 3.45 ± 1.21, p-value=0.41).

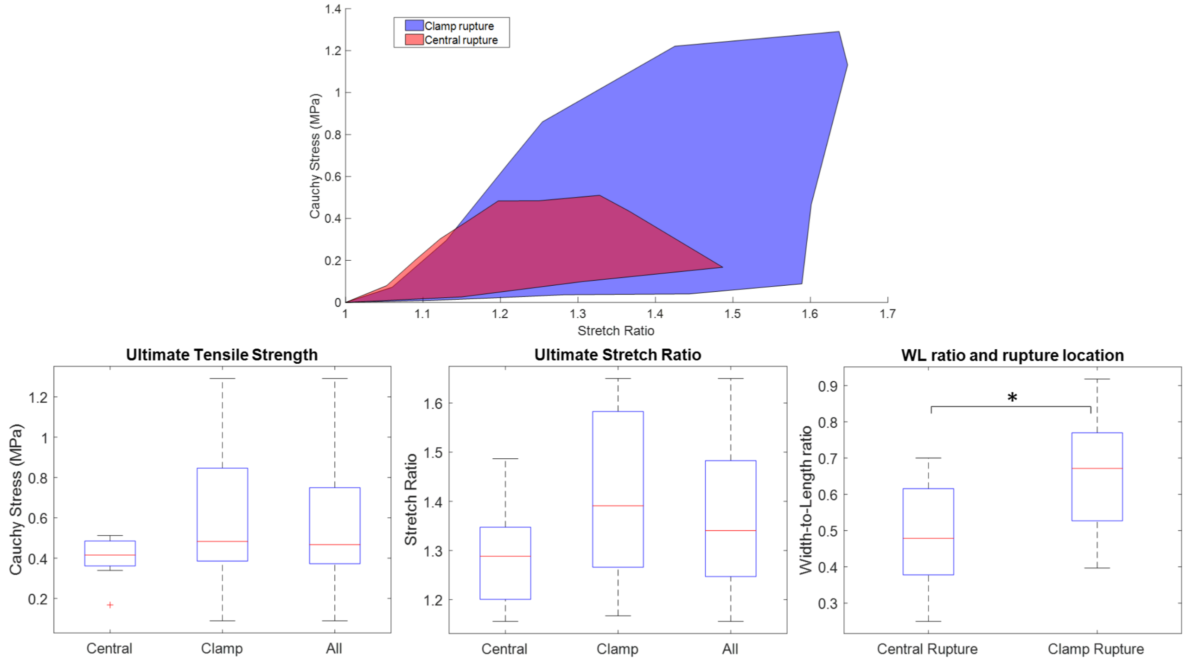

Figure 3.10: Above, Cauchy stress vs Stretch ratio data range of CEA specimens grouped by location of rupture. Below, Box plots (median – red line, IQR - box and range) and showing statistics of ultimate tensile strength, ultimate stretch ratio and WL ratio per group (central rupture, clamp rupture and all). * = p-value < 0.05.

3.2.3. Relation to global collagen structural properties

The global mechanical parameters of each non-calcified CEA strip obtained through uniaxial tensile tests were compared against the global (averaged) collagen structural parameters derived from the corresponding MPM-SHG images, to assess the possible existence of correlations between them.

Independent t-tests on the mechanical properties of groups based on mean predominant fiber angles (strips with average μ_p between ±20°, and the rest) (Fig. 3.2) did not show any significant differences. Correlation coefficients (ρ) and p-values from the Spearman's correlation tests between all global mechanical and global structural parameters described above are presented in Table 3.1. For evaluating the influence of the global predominant fiber angle on the global mechanical properties, the mechanical results were compared to μ_{pcirc} (Fig. 3.3), and to the standard deviations of μ_p (variability in predominant angles within each strip) (bars of Fig. 3.2). As observed in Table 3.1, the only significant correlation was found between the stretch ratio at the inflection point and the fiber dispersion level within the sample, indicated by the mean σ_p in the fiber angle histogram (ρ= 0.39, p-value=0.03).

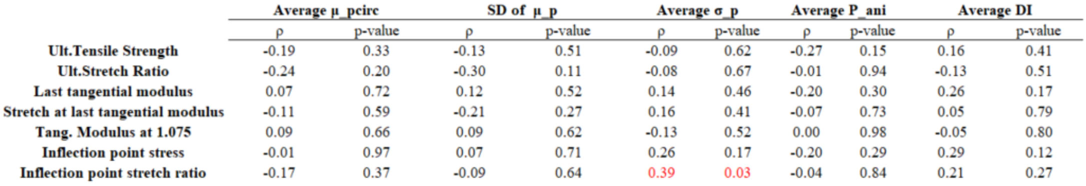

	Average μ_pcirc		SD of μ_p		Average σ_p		Average P_ani		Average DI	
	ρ	p-value	ρ	p-value	ρ	p-value	ρ	p-value	ρ	p-value
Ult.Tensile Strength	-0.19	0.33	-0.13	0.51	-0.09	0.62	-0.27	0.15	0.16	0.41
Ult.Stretch Ratio	-0.24	0.20	-0.30	0.11	-0.08	0.67	-0.01	0.94	-0.13	0.51
Last tangential modulus	0.07	0.72	0.12	0.52	0.14	0.46	-0.20	0.30	0.26	0.17
Stretch at last tangential modulus	-0.11	0.59	-0.21	0.27	0.16	0.41	-0.07	0.73	0.05	0.79
Tang. Modulus at 1.075	0.09	0.66	0.09	0.62	-0.13	0.52	0.00	0.98	-0.05	0.80
Inflection point stress	-0.01	0.97	0.07	0.71	0.26	0.17	-0.20	0.29	0.29	0.12
Inflection point stretch ratio	-0.17	0.37	-0.09	0.64	0.39	0.03	-0.04	0.84	0.21	0.27

Table 3.1: Correlation results from the Spearman's tests (correlation coefficient ρ and p-value) between global collagen structural parameters (axis above) and global mechanical properties (left axis). In red, statistical significant correlations.

3.3. Local mechanical properties

After uniaxial tensile tests of the CEA strips, the local mechanical (deformation) characteristics of those that exhibited a clear rupture initiation in the central region, were studied under 2D Digital Image Correlation analysis. Strain patterns (or fingerprints) at the rupture region immediately before rupture initiation were investigated to examine potential mechanisms of rupture. Subsequently, the deformation results from DIC analysis (DIC-based) were later compared to the global results from gauge length (GL)-based analysis, to spot differences between local and global-based deformation analysis methods. Finally, the collagen structural characteristics of the rupture, high and low strain regions were examined to determine possible structural vulnerable properties.

A total number of 11 ruptures from 10 samples were assessed. Out of the 11 ruptures, seven of them progressed to be the main rupture (that lead to complete rupture of the tissue), and 4 of them were the first visible rupture in the tissue that did not result in a complete rupture of the specimen. A representative case is presented in Fig. 3.11 (Nr. 1). As for this case, generally the moment of rupture initiation (represented by the "Rupture frame") did not correspond to a noticeable change in the stress-strain curve. It was also noted for all the strips that from the moment when rupture initiated, irregularities started to appear in the curves and the stiffness decreases, as can be seen in Fig. 3.11 (Nr. 2, 3). Rupture progression was gradual for all cases.

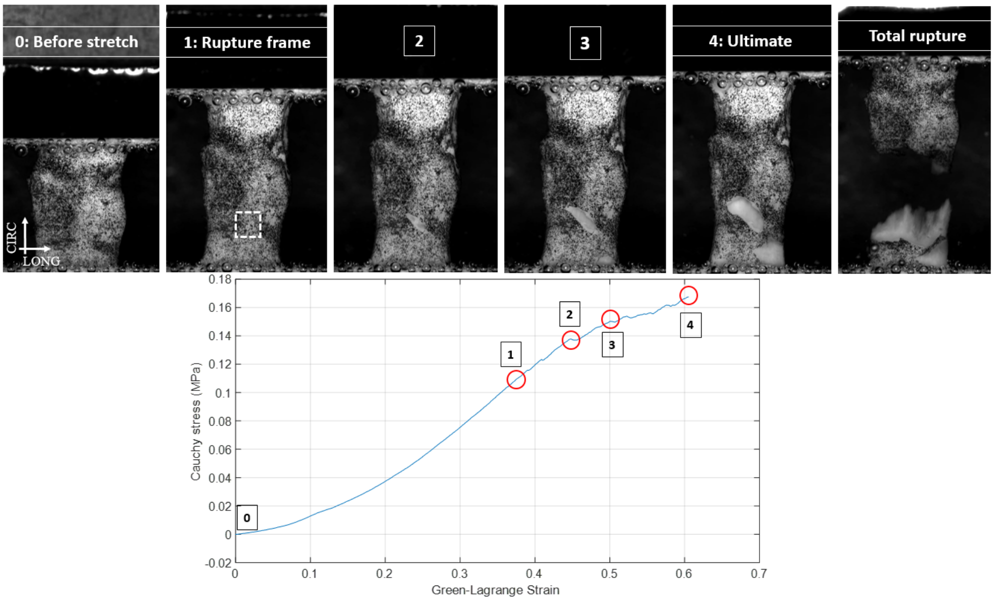

Figure 3.11: Tensile test procedure and rupture progression of a CEA sample with corresponding stress-strain curve (bottom). 0) Pre-stretched state. 1) Rupture initiation, frame immediately before rupture (white square), which was the focus of DIC analysis. 2) and 3) Rupture progression associated to irregularities in the stress-strain curve. 4) Moment corresponding to ultimate strength and strain parameters extracted through traditional methods. 5) Total rupture of the tissue.

3.3.1. Digital Image Correlation results

The DIC analysis results of the “Rupture frames” in the form of Green-Lagrange strain distribution maps (tensile, shear and longitudinal) of all the ruptures (n=11) are displayed in Fig. 3.12. By obtaining the statistics of the strain values at the rupture regions (white squares in Fig. 3.12) and the whole ROI, and carrying out visual observations of the results, three recurrent strain fingerprints at the rupture regions were identified:

- **Tensile strains** (see Fig. 3.13): In all the specimens, high tensile strain values, compared to the average of the ROI, were found at the rupture region. In particular, in 5 out of 11 (Samples 518-1, 523-2, 539-1, 543-1, and 549-2) the maximum tensile strain value within the whole strip was detected there, while the other 6 cases (Samples 525-1, 540-1, 542-1, 544-2, 546-2.1, 546-2.2) showed a local maximum value. The mean ± SD of the average Green-Lagrange strain within the whole ROI (orange bar in Fig. 3.13) was 0.14 ± 0.05, which was significantly lower (p-value=0.03) than the average strain in the rupture regions (yellow bar in Fig. 3.13): 0.24 ± 0.13. The mean ± SDs of the maximum strain values within the rupture regions (purple bar in Fig. 3.13) and within the whole ROI were 0.41 ± 0.35 and 0.56 ± 0.49, respectively. These were also significantly higher than the averaged strains within the ROI (p-value=0.02 and 0.01). Interestingly, this same trend of higher strains at the rupture region was observed in the physiological frames (see Appendix 6.0.4)
- **Shear strains**: Nine out of 11 rupture regions analyzed (Samples 518-1 ,523-2, 539-1, 540-1, 543-1, 544-2, 546-2.1, 546-2.2, and 549-2) exhibited a valley in the shear strain values (transition from negative to positive values). Four of them located exactly at the point of rupture initiation whereas the other five near the ruptured spot, within the rupture region.
- **Longitudinal strains**: Finally, 7 rupture regions (Samples 518-1, 525-1, 540-1, 542-1, 543-1, 544-2, 546-2.1, and 549-2) exhibited the lowest longitudinal strain value of the whole ROI. The mean ± SD of the minimum strain values at the rupture regions was -0.25 ± 0.07, while the mean ± SD of the average strain within the whole ROI was -0.15 ± 0.05.

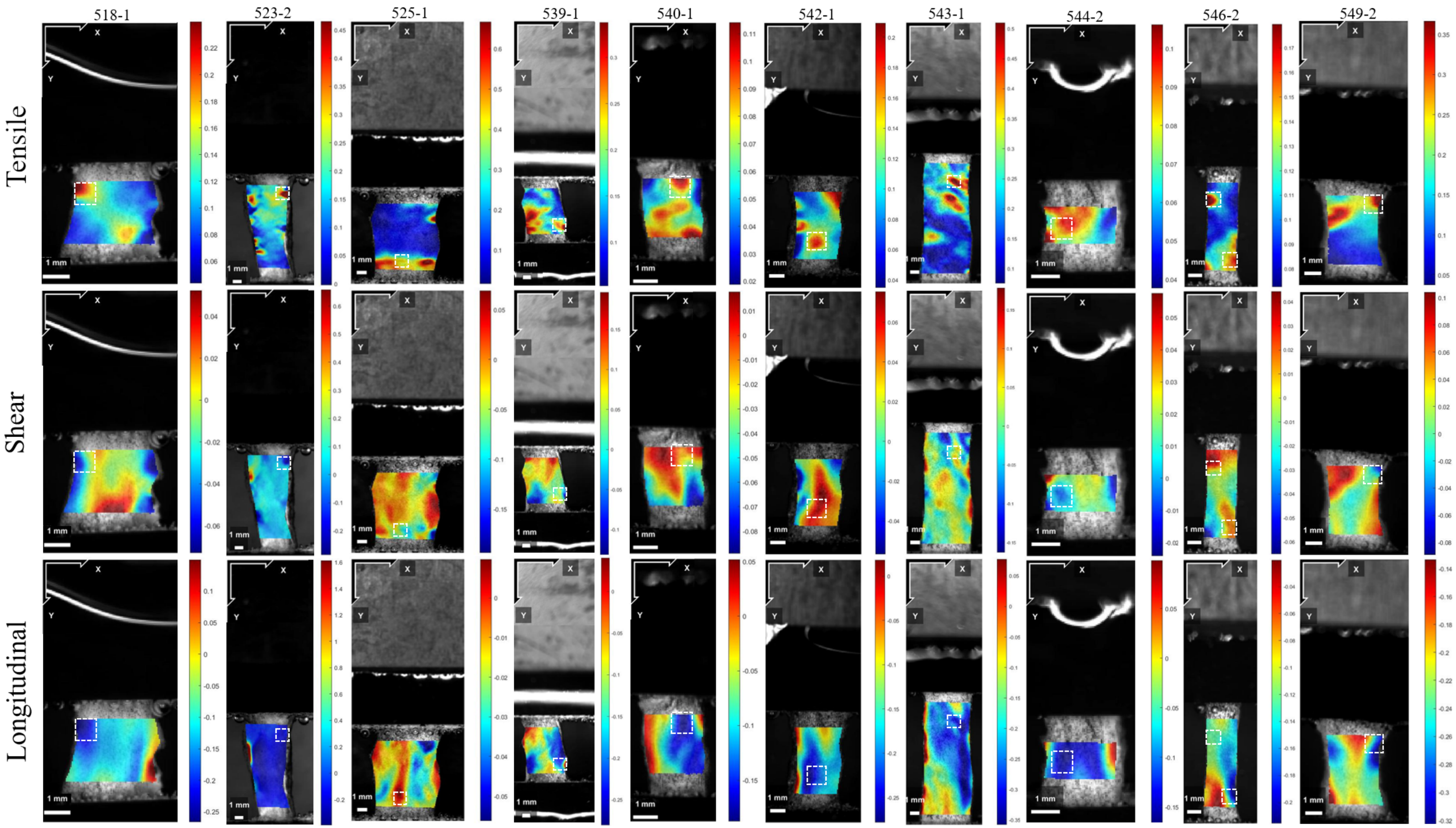

Figure 3.12: Green-Lagrange strain distributions for all the samples (tensile, shear and longitudinal) at the rupture frame. Rupture region is indicated as white squares within the ROI. X- and Y-axis correspond to longitudinal and circumferential directions respectively.

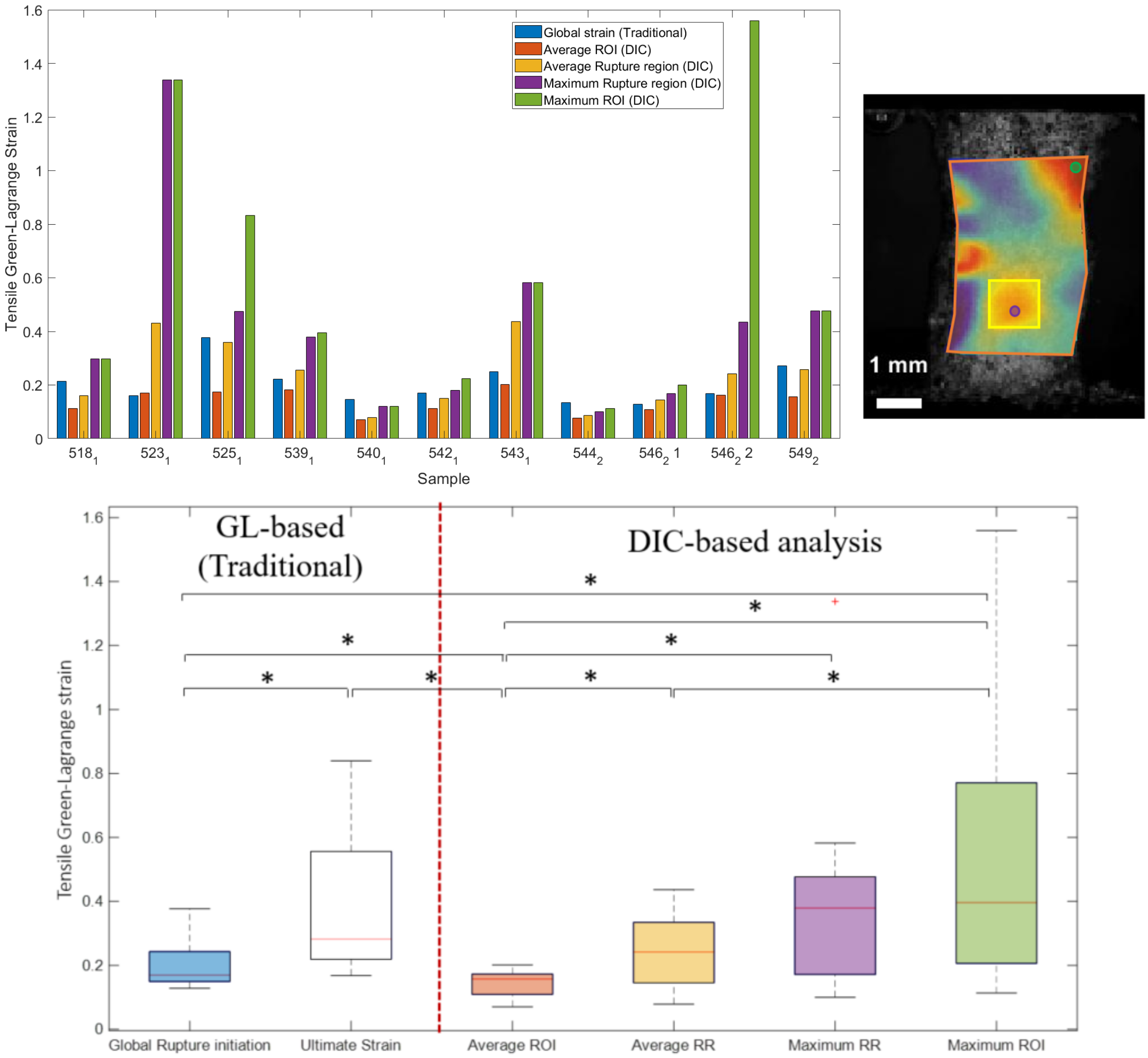

Figure 3.13: Plots of Green-Lagrange tensile strains at the Rupture frame: Top-left) Bar graph with values for all the samples analyzed. Top-right) DIC tensile strain map from Sample 542-1 showing analyzed regions at the rupture frame. Bottom) Boxplots with averages, separated in GL-based (left) results and DIC-based results (right). Blue: Global strain at rupture initiation from (GL-based). White: Ultimate strain (GL-based). Orange: Average strain of whole ROI (DIC-based). Yellow: Average strain at the rupture region (RR) (DIC-based). Purple: Maximum value of strain at the Rupture region (DIC-based). Green: Maximum value of strain at the whole ROI (DIC-based). *p-value<0.05

GL-based assessment revealed the average, global tensile strain properties of the CEA strips at the rupture initiation (mean ± SD: 0.20 ± 0.07)(blue bar in Fig. 3.13), and the ultimate strain values at tissue complete disruption (0.38 ± 0.22) (white bar in Fig. 3.13), which were significantly higher than the former (p-value=0.02).

DIC analysis enabled local assessment of the highly non-uniform, heterogeneous strain distribution. The averaged DIC-based ROI tensile strains at the rupture initiation (orange bar in Fig. 3.13) was significantly lower than the global GL-based measurements (blue bar in Fig. 3.13) (p-value=0.022). However, DIC-based average and maximum strain values of the rupture region (yellow and purple bars in Fig. 3.13) were higher than the previous measurement. Furthermore, the DIC-based maximum strains at the rupture region and at the whole ROI (green bar in Fig. 3.13) were higher than the ultimate GL-based tensile strains.

The impact of the choice of the type of strain measurement (DIC-based vs. GL-based) is further illustrated with a representative case (Fig. 3.14). It shows distinct stress-strain curves until rupture initiation. The material seems to have softer (more compliant) material behavior when the GL-based strains are examined instead of more accurate DIC-based ROI average strains. The maximum and minimum DIC-based strain values (dashed lines in Fig. 3.14) showing the strain range, illustrate the heterogeneity of the strains present in the luminal surface of the strips, which is not perceived by traditional gauge length-based methods.

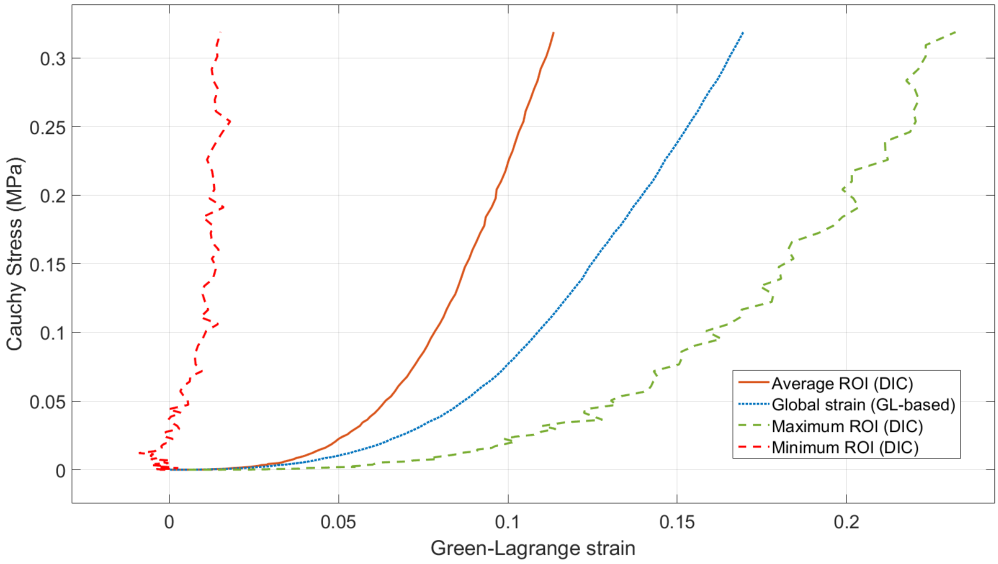

Figure 3.14: Stress-strain curve of strip 542-1 displaying the different tensile strains measured until rupture initiation: Global gauge length-based global strains (blue dotted line), the average DIC-based strain of the ROI (solid orange line) and the maximum and minimum DIC-based strain values of the ROI (dashed green and red lines).

3.3.2. Relation to local collagen structural properties

Rupture, high and low tensile strain regions (n=10, 17 and 27) from the strips analyzed under DIC (n=10) were studied at the “Rupture frames” to evaluate the association of the collagen microstructure with local mechanics in the loading direction. One strip was excluded from the analysis (523-2) because the rupture region was not captured through the MPM-SHG.

μ_{pcirc} was observed to be significantly higher (p-value=0.0013) at the regions that suffered high strains (average ± SD: 35.15 ± 24) compared to those that underwent low strains (average ± SD: 15.83 ± 13), as seen in Fig. 3.15. Although the rupture regions showed high tensile strains (3.3.1), their μ_{pcirc} distribution (average ± SD: 20.9 ± 14) was not significantly higher than the low strain regions. When the rupture region values were combined with the high strains, the difference with respect to the low strain regions was still significant. No other trends were observed between these regions with respect to dispersion collagen parameters.

Furthermore, due to the structural heterogeneity of the strips, collagen parameters at the rupture regions were compared to the averaged collagen parameters, as in Fig. 3.16. No interesting trends were observed.

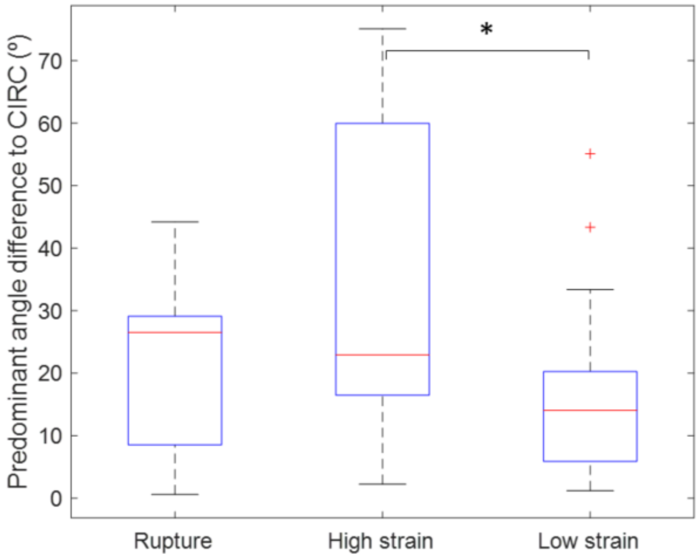

Figure 3.15: Distributions of the predominant angle difference from the circumferential direction data per local regions.

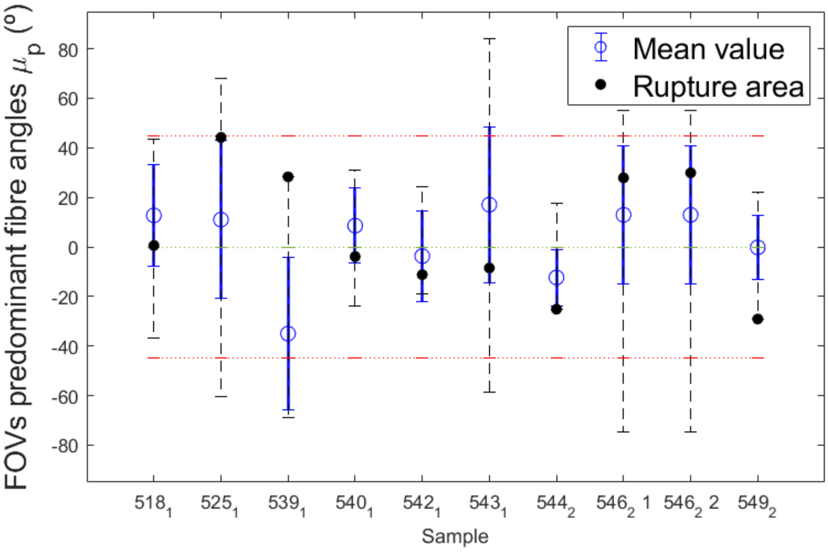

Figure 3.16: FOVs predominant fiber angles: mean and rupture regions (ranges – dashed bars, standard deviation-solid bars)

4

Discussion

This study focused on enhancing our understanding of atherosclerotic plaque mechanics, structure and rupture. This was done by characterizing the collagen network of non-calcified carotid plaque tissues through MPM-SHG imaging, as well as their global and local mechanical responses under uniaxial tensile tests. Apart from studying these properties individually, the relations between them were investigated in order to evaluate the influence of collagen architecture on the mechanical properties and compare the local and global mechanical results extracted through DIC analysis and traditional gauge-length analysis, respectively.

4.1. Collagen structural properties

The 2D quantitative analysis of MPM-SHG images from the luminal side of the test strips (n=31) showed that the collagen fibers were predominantly oriented closer to the circumferential direction of the arteries (in 87 % of the FOVs) than to the longitudinal direction (see Fig. 3.2 and 3.3). Only three strips (9%) had a predominantly longitudinal fiber orientation in overall. Additionally, the distributions of predominant angles showed a large intra-sample variation in fiber orientation (average SD: 21°) with ranges up to 150° (representative case Fig. 3.1), manifesting the heterogeneous nature of atherosclerotic plaques. With atherosclerosis progression, SMCs that migrate from the tunica media into the diseased intima produce the collagen of the fibrous plaque, and, according to the results in this study, preferentially towards the circumferential direction, as it is the case for the collagen in the tunica media of healthy arteries. Since the main mechanical loading and deformation due to the intraluminal blood pressure is in the circumferential direction, the preferred orientation of the fibers along this direction, may contribute to the load-bearing capacity of the plaque tissue in vivo, and therefore to its stability [15], as it is the case in healthy arteries [16].

The fiber orientation results of this study slightly differ from those of *Johnston et al.*, who reported that 40% of the carotid fibrous caps, imaged with Small Angle Light Scattering (SALS), were seen to have a predominantly circumferential fiber orientation [11]. These authors also reported lower intra- and higher inter- sample variabilities than the current study. *Akyildiz et al.*, who imaged the 3D collagen structure of complete CEA through Diffusion Tensor Imaging (DTI), showed that 50% of the collagen fibers are oriented towards the circumferential direction [15]. The heterogeneity of plaques, the distinct disease stages and regions analyzed, and the variations between the imaging techniques employed might contribute to the differences among these studies and the current study. In the end, these variations in the orientation results indicate that rupture risk assessment and treatments should strive to be plaque-specific, by imaging plaque components characteristics for their integration into computational models, when their influence on the mechanics would be completely elucidated.

Results from σ_p and P_{ani} indicated that the majority of areas had a collagen fiber organization with a certain level of dispersion, while still having a preferred orientation (not completely isotropic due to the presence of a peak). Again, as with the predominant orientation, high intra-sample variability was observed, which was comparable from strip to strip. Similarly, *Douglas et al.* reported for coronary plaques different levels of fiber dispersion, depending on the area, leading to a large range of values [43]. In general, there is not much information in the literature about the dispersion of the collagen fibers in atherosclerotic plaques, and studies that report this fiber structural property in cardiovascular tissues, employ different indices, complicating the comparisons. A new dispersion index was introduced in this study as a combination of the original parameters obtained from the Gaussian distributions, to permit a direct examination of this property. However, the usefulness of this index needs future research.

Interestingly, a negative correlation between the angle difference to the circumferential direction and the anisotropic fraction was noted when evaluating the collagen networks of all the FOVs. This relation indicates that the more longitudinally oriented the fibers are regionally, the more disperse is their distribution. A link between these two properties has not been reported before for atherosclerotic plaques.

4.2. Global mechanical properties

The global mechanical properties of the imaged non-calcified plaque strips in the circumferential direction were characterized through uniaxial tensile testing until failure, and subsequent traditional force versus displacement (gauge length-based) analysis. The results showed that tissues exhibited non-linear mechanical behavior and demonstrated the high variability among plaques (Fig. 3.8), as seen in many previous studies for plaque tissues [13][40][44][45][11].

4.2.1. Pre-failure properties

The stiffness calculated at different stretch levels, in the form of tangential modulus, further details the global mechanical behavior of plaque tissue, and demonstrates the high inter-sample variability (Fig. 3.9). Generally, a strain stiffening behavior was observed for the plaque tissue. This behavior could be attributed to the progressive recruitment of collagen fibers. This is a well-established phenomenon in healthy arteries [16], where at low strain levels, collagen fibers remain undeformed in a wavy state, and the elastin fibers bear the load. Upon larger load application (*i.e.* greater intraluminal pressure), the load bearing task is transferred from elastin fibers to collagen fibers, which are recruited and straightened, leading to a stiffness increase, as they are generally stiffer [16][10]. The average stiffness values were observed to decrease from a stretch ratio of 1.35 onwards, which might be attributed to the gradual damage in the tissue due to the increased number of failed collagen fibers.

The stiffness results presented here are in accordance with the tensile stiffness values from several other experimental papers on plaques discussed in the review of *Akyildiz et al.* [10]. The average stiffness values found in the current study fall in the middle of the range reported in this review (30 kPa to 270 MPa), similar to those from *Maher et al.*, who also tested CEA samples in the circumferential direction [45]. The review stated a great dispersion in the results between and within the studies, indicating a large biological variation for atherosclerotic plaques [10], as also observed in the current study.

In addition to the stiffness, the inflection points of the stress-stretch curves were investigated, considering them as those points where the change of slope was maximum. The interest of identifying these points relied on the hypothesis that in arteries, it is the deformation where collagen fibers start engaging and taking over the mechanical response [46][39][47]. Nonetheless, no previous study on atherosclerotic plaques have reported about inflection points; only in healthy arteries [48] and aneurysms, where they were related to the progression state of the disease [46]. It is also important to note that this point is rather symbolic and not a tangible parameter, proof of which is the existence of different methods to calculate it [48][39].

4.2.2. Failure properties

The rupture behavior of plaques was examined by obtaining the stress and stretch at the ultimate tissue failure. The UTS (ultimate tensile strength) and USR (ultimate stretch ratio) average values for all samples were 0.55 ± 0.32 MPa and 1.38 ± 0.15, respectively. UTS values were seen to be higher but comparable to the values reported in the studies of *Cunnane et al.*, *Maher et al.*, and *Lawlor et al.*, who also tested CEA samples in the circumferential direction: 0.49, 0.40, and 0.37 MPa, respectively [29][45][13]. Apart from this, in general, the results of strength presented here were higher than values reported for different plaque specimens (different location, parts, etc.) in several papers [44][22][40][49]. Ultimate strength has been commonly proposed and regarded as a vulnerability factor (unlike USR), and some studies have employed 0.3 MPa as a threshold value for plaque models [44]. However, the results presented in this project and in some of the above-mentioned have revealed higher UTS than the value proposed, suggesting that more complete investigations of the characteristics of plaques should be performed for establishing such a threshold. The specifically high UTS obtained in the current project might be explained by the tissue type, the lack of calcifications and the thickness measurements through ultrasound imaging. Firstly, carotid plaques have been seen to withstand higher stresses compared to other plaque types (such as femoral in [50]). Secondly, calcifications have been demonstrated to reduce the load-bearing capacity of diseased arterial tissues as in some studies the UTS for calcified tissues was lower than non-calcified or non-predominantly calcified [44][50]. In the current study, they were avoided to focus on the effect of collagen. Finally, the plaque ultrasound thickness measurements carried out in the pre-stretch state of the specimens, were observed in this study to give significantly lower values than the commonly used methods of quantifying thickness at the undeformed state. The thickness reduction supposes an increase of the calculated stress for the whole procedure. In this sense, the use of ultrasound imaging for more accurate thickness measurements at the pre-stretch state is recommended for further experiments.

On the other hand, the USR values reported in the current project (1.38 ± 0.15) are within the large range of values extracted from previous studies: 1.4 in *Maher et al.* [45], 1.2 in *Lisicky et al.* [44], 1.49 in *Lawlor et al.* [13] or 1.89 in *Cunnane et al.* [29].

Regarding the location of rupture, only eight of the CEA strips ruptured at the central region, compared to 21 at the clamp region. No statistically significant differences in ultimate parameters between the two groups were noted, although a higher variability in the UTS results was observed in clamp ruptured samples (Fig. 3.10). *Cunnane et al.* and *Lisicky et al.* made the same observations between samples grouped based on their rupture location: they did not show significant differences in terms of their mechanical characteristics [44][50].

Overall, the global mechanical properties acquired in this project are in accordance with results in literature. However, the great variation in the stiffness and ultimate parameters across and within the studies demonstrate the strong need to further deepen our understanding of plaque tissue behavior and rupture characteristics, and their link to the tissue structure, if possible locally. Especially, the role of the collagen fiber orientation is unknown, as stated in *Davis et al.* [22], and therefore, it was investigated in this study.

4.2.3. Relation to global collagen structure

In general, no statistically significant correlations were observed between the global mechanical parameters and the averaged collagen parameters of the strips. Solely a statistically significant positive correlation was found between σ_p and the stretch level at the inflection point. This positive correlation indicates that the more dispersed the collagen fibers within a sample are, the greater is the stretch where the inflection point is reached.

Contrary to the findings of the current study, *Johnston et al.* found a significant correlation between the collagen fiber orientation and the global mechanical properties of fibrous plaque caps: the caps which had predominant fiber orientation closer to the loading direction (circumferential), withstood higher stresses before failure, and underwent lower strains (stiffer) [11].

In this regard, a limitation that would possibly contribute to the different results obtained in this study is that the collagen information was acquired only from the top, luminal part of the samples. The imaging depth of MPM-SHG was limited to 0.15 mm, whereas the average thickness of the strips was 1.2 mm. According to *Akyildiz et al.,* the collagen fibers in deeper layers of the plaques could possibly be differently oriented than the ones close to the lumen [15]. *Johnston et al.* tested only fibrous caps whose thickness (0.54 mm) was less than half the thickness of the samples employed in the current study, thus getting rid of the contribution of underlying layers of the plaques. That way, SALS acquired collagen information from throughout the whole thickness of the specimens.

Furthermore, the high inter-sample variation in the orientation results allowed *Johnston et al.* to classify the samples into two opposing groups: predominantly circumferential and longitudinal fiber orientation, from which they obtained the different mechanical behaviors. In the current study, the majority of the samples exhibited a predominantly circumferential fiber orientation, hence probably leading to undetectable differences for the type of analysis performed. In addition, the important intra-sample variability in all the collagen structural parameters seen in the current study would further indicate that the type of analysis employed, based on averaging the parameters measured in each sample, might not be effective for investigating this relation, since it may overlook the heterogeneity of the samples. Instead, in order to evaluate better the influence of the collagen fiber organization, a more localized analysis of certain areas of the plaques, where the fiber structure would not vary significantly, should be performed. This was carried out in this study through local mechanical analysis by means of DIC.

4.3. Local mechanical properties

4.3.1. Strain fingerprints

The local strain characteristics at the luminal side of atherosclerotic plaques under uniaxial tensile testing were, for the first time, exhaustively analyzed. The strain distributions (Fig. 3.12) clearly exhibited the heterogeneous nature of these tissues. Concretely, the local strain characteristics leading to rupture were evaluated. To achieve this, the DIC analysis employed in this study was performed following a new methodology, since the current literature on the analysis of local strains with DIC mainly addresses non-biological tissues. The methodology employed here is therefore proposed for future experiments with biological tissues.

In this regard, it was observed that for all samples, the initiation of the ruptures occurred at significantly lower strains and stresses than the ultimate parameters (USR and UTS), which have been commonly the focus in mechanical studies. Therefore, in this study, the local strain analyses were focused especially on the regions where rupture was initiated, which were detected visually.

An important finding of the current study is that all rupture regions exhibited local high tensile strain (immediately before rupture); where for 46% of them it was also the maximum strain of the entire ROI. Interestingly, this trend was also observed at the physiological deformation levels. This observation indicates that the high rupture risk areas may be detected even at low strain levels. In this sense, the strain could serve as a predictive metric for rupture, as also was proposed earlier by *Davis et al.* and *Johnston et al.* [22][11].

In addition to the high tensile strains, shear strain valleys (transitions from negative to positive values) and low longitudinal strains were detected in 81% and 63% of the rupture regions, respectively. However, these observations would need further experiments to check their validity and to elucidate their mechanical meaning. Also, note that shear strains should be absent in tensile tests; however, their presence in the plaques are mainly due to the structural heterogeneity of the tissue.

4.3.2. Gauge length-based strain analysis method vs DIC

The comparison between the global gauge length-based strain assessment (traditional method), typically employed in previous studies, and the DIC-based strain measurements (Fig. 3.13), showed that the former overestimates the overall average strain in the central region. This is likely due to the fact that the traditional method includes the near-clamp regions, which show considerably greater strains than the central region because of the clamping effects (see Appendix 6.0.5). Additionally, and most importantly, GL-based strains were seen to underestimate tissue rupture strain.

From these experiments and analyses performed, it is inferred that the global GL-based strain assessments do not capture the heterogeneous deformation characteristics of the plaques, illustrated by the range of strains seen in Fig. 3.14, nor characterize accurately the rupture strain. DIC analysis on the other hand, demonstrated to be a powerful tool for assessing the heterogeneity of the tissues and for providing precise measurements at rupture regions. As a consequence, its use is remarkably recommended for future experiments on biological tissues.

4.3.3. Relation to local collagen structure

To solve the drawbacks of the global methods when investigating the role of collagen in plaque mechanics, the collagen structural parameters acquired at different local strain regions and at the rupture regions were evaluated. Although MPM-based collagen parameters were acquired with a low imaging depth, their combination with DIC results was justified as the latter also examines the luminal surface of the samples.

Interestingly, the predominant fiber angle difference to the circumferential direction was observed to be significantly higher (p=0.0013) in high strain areas compared to low strain areas (Fig. 3.15). This suggests that the collagen fiber orientation relative to the loading direction affects the local strain level, in a way that areas of the tissue with fibers less oriented towards the loading direction would undergo higher strains than areas with fibers more oriented towards that direction.

Moreover, it could also indicate that collagen fiber orientation would determine the local strength as it was observed that the rupture regions were also high strain regions. However, this hypothesis needs direct investigations. Possibly, there are more factors apart from collagen fiber orientation implicated in the strength of the plaques. A proof of this is that many regions that exhibited high strains (even higher than rupture regions) did not rupture, while no significant differences in the collagen structure were seen between them and the rupture regions.

This conclusion matches with the above-mentioned observations that *Jonhston et al.* found when investigating the relationship between the global mechanical and structural properties of plaque caps. They detected that samples with fibers predominantly aligned away from the loading direction ruptured at lower stresses and higher strains than the samples with fibers predominantly oriented towards the loading direction [11]. The present study presumably corroborates that relation regarding the strain, and in local areas, which is important to highlight.

4.4. Limitations and Future recommendations

The samples were tested only in the circumferential direction under uniaxial tensile testing conditions. Circumferential tensile stretch is the predominant deformation in the arterial vasculature *in-vivo*; hence, the tests performed in this study possibly provide the most important and mechanically relevant information. Yet, additional mechanical tests such as uniaxial tensile tests in the longitudinal direction or biaxial tensile tests can provide useful extra information for a more comprehensive understanding of mechanical and rupture characteristics of plaque tissue

Given the main focus of studying the collagen role, calcifications were avoided in the samples. However, calcifications are considered to affect the stress-strain distribution in atherosclerotic plaques [51]. It should be noted that the current study provides a better understanding of fibrous plaque tissue characteristics and the translation of this acquired knowledge to the *in-vivo* plaque rupture should be done cautiously.

The local strain distribution in the plaque tissue was, for the first time, exhaustively studied here. No assumptions such as the homogeneity of the structure or of the strain distribution were needed for the analysis. Conclusions about the rupture of the plaques were rendered from these analyses. However, for the stress analyses it was assumed that stresses were homogeneously distributed. The analysis of local stresses through local stiffness evaluations and local thickness measurements could provide more complete results about the mechanical response of these tissues.

On the other hand, due to the high amount of strips that ruptured at the clamps, only 11 ruptures out of 31 strips could be analyzed through DIC, as the analysis of near-clamp areas was observed to not be precise. In general, the clamps of the tensile tester induce high stresses that can lead to sample rupture that would not be related to the biological properties. Better experimental designs that will enhance central region rupture will increase the number of ruptures analyzed. To achieve central rupture, ASTM recommends dogbone shapes (instead of rectangular) with long central regions where there would be relatively higher stresses [52]. Dogbone shapes are difficult to obtain with plaque samples, due to the risk of damaging the tissue while dissecting. Alternatively, as it was demonstrated in the current study, rectangular samples with lower WL ratios are more prone to central rupture; hence, further studies should strive to get slender specimens.

Furthermore, the rupture initiation location was identified visually, which is not ideal. An objective and automated rupture detection tool could be developed in the future by using DIC strain measurements and analyzing the discontinuities on the strain distribution. However, such an effort was considered beyond the scope of the current study.

Collagen imaging through MPM-SHG provided high resolution images from the strips. Due to the long imaging times required, not the entire test samples but selected regions (40% of the total sample area) in the samples were imaged. The results acquired were sufficient to demonstrate the heterogeneous structure of the plaque tissue and relate this to the local mechanical strains. However, some rupture regions were between the imaged regions and therefore the collagen structural parameters related to such rupture regions were obtained from the closer imaged region. Some other, recently developed techniques such as polarized spatial frequency domain imaging (pSFDI) could provide the structural information much faster than MPM-SHG, hence allowing the scan of the entire sample area and the load-dependent collagen behavior if integrated into the mechanical set-ups.

5

Concluding remarks

The main findings of this research are elaborated below based on the aims of the study:

- The collagen fiber orientation and dispersion of the luminal side of atherosclerotic fibrous plaques were successfully characterized non-invasively by means of MPM-SHG. The majority of the collagen fibers (87%) were seen to be predominantly oriented towards the circumferential direction of the artery, with a certain level of dispersion. Yet, the collagen structural parameters (predominant angle and the dispersion) showed a substantial intra-sample variation representing the high heterogeneity of plaque tissues regionally. A correlation between the predominant fiber angle and the level of the dispersion of the fibers was discovered: the more away from the circumferential direction the predominant angle was in a region, the more dispersed were the fibers there.
- The mechanical responses of the imaged non-calcified fibrous plaques under uniaxial tensile testing in the circumferential direction of the artery were characterized successfully. The global mechanical results, obtained through traditional gauge length-based deformation measurements, demonstrated the non-linear stress-strain behavior, typical to many soft biological tissues. A large variation in the pre-failure and failure parameter values from these analyses was observed. Moreover, the relation between the averaged collagen structural parameters and the global mechanical responses of the plaques did not yield significant correlations. These findings were probably due to the structural heterogeneity of the plaque tissue and hinted towards a local analysis for a more comprehensive understanding.
- The subsequent local strain analysis, obtained with Digital Image Correlation, showed that the rupture regions exhibit significantly high tensile strains before rupture initiation. This implies that the local strain could serve as a predictive metric for plaque rupture. The comparison between the global and local techniques rendered that the former may overestimate average central region strain while underestimating tissue rupture strain. The local investigations showed a relation between the regional tensile strain and the regional predominant collagen fiber orientation relative to the circumferential direction, suggesting that areas of the tissue with fibers less oriented towards the loading direction would undergo higher strains than the areas with fibers more oriented towards that direction. Based on this, it was hypothesized that collagen fiber orientation relative to the loading direction could influence the regional vulnerability of the plaques.

This current study showed that the combined local analysis of the mechanical and structural properties may serve to greatly improve our knowledge towards understanding plaque rupture. This analysis is able to address the heterogeneity of the tissues, investigating more accurately the role of every plaque constituent (in this case, collagen) and therefore overcoming the large variations observed in the global mechanical responses. Further experiments following this will have the potential to improve computational models in the search for better rupture risk assessment and treatment planning, for eventually preventing acute cardiovascular events, such as myocardial infarctions or strokes.

References

[1] WHO, *Cardiovascular diseases*, 2021.

[2] A. M and Y. KS, "Pathogenesis of Atherosclerosis A Review," *Medical & Clinical Reviews*, vol. 2, no. 3, Aug. 2016.

[3] F. E, "Pathogenesis of atherosclerosis," *Journal of the American College of Cardiology*, vol. 47, no. 8 Suppl, Apr. 2006.

[4] A. Taki, A. Kermani, S. M. Ranjbarnavazi, and A. Pourmodheji, "Overview of Different Medical Imaging Techniques for the Identification of Coronary Atherosclerotic Plaques," *Computing and Visualization for Intravascular Imaging and Computer-Assisted Stenting*, pp. 79–106, Jan. 2017.

[5] S. K. Nadkarni, B. E. Bouma, J. De Boer, and G. J. Tearney, "Evaluation of collagen in atherosclerotic plaques: The use of two coherent laser-based imaging methods," *Lasers in Medical Science*, vol. 24, no. 3, pp. 439–445, May 2009.

[6] P. Libby, J. E. Buring, L. Badimon, *et al.*, "Atherosclerosis," *Nature Reviews Disease Primers 2019 5:1*, vol. 5, no. 1, pp. 1–18, Aug. 2019.

[7] A. C. Newby and A. B. Zaltsman, "Fibrous cap formation or destruction — the critical importance of vascular smooth muscle cell proliferation, migration and matrix formation," *Cardiovascular Research*, vol. 41, no. 2, pp. 345–360, Feb. 1999.

[8] O. Ovchinnikova and Larserics Digital Print), "Immune mechanisms behind plaque vulnerability: experimental and clinical studies," Nov. 2010.

[9] J. (of applied mechanics) Ohayon, G. Finet, and R. Pettigrew, "Biomechanics of coronary atherosclerotic plaque : from model to patient," 2020.

[10] A. C. Akyildiz, L. Speelman, and F. J. Gijsen, "Mechanical properties of human atherosclerotic intima tissue," *Journal of biomechanics*, vol. 47, no. 4, pp. 773–783, Mar. 2014.

[11] R. D. Johnston, R. T. Gaul, and C. Lally, "An investigation into the critical role of fibre orientation in the ultimate tensile strength and stiffness of human carotid plaque caps," *Acta biomaterialia*, vol. 124, pp. 291–300, Apr. 2021.

[12] M. T. Walsh, E. M. Cunnane, J. J. Mulvihill, A. C. Akyildiz, F. J. Gijsen, and G. A. Holzapfel, "Uniaxial tensile testing approaches for characterisation of atherosclerotic plaques," *Journal of Biomechanics*, vol. 47, no. 4, pp. 793–804, Mar. 2014.

[13] M. G. Lawlor, M. R. O'Donnell, B. M. O'Connell, and M. T. Walsh, "Experimental determination of circumferential properties of fresh carotid artery plaques," *Journal of biomechanics*, vol. 44, no. 9, pp. 1709–1715, Jun. 2011.

[14] C. CK, S. L, O. CW, and B. FP, "Compressive mechanical properties of atherosclerotic plaques–indentation test to characterise the local anisotropic behaviour," *Journal of biomechanics*, vol. 47, no. 4, pp. 784–792, Mar. 2014.

[15] A. C. Akyildiz, C. K. Chai, C. W. Oomens, *et al.*, "3D Fiber Orientation in Atherosclerotic Carotid Plaques," *Journal of Structural Biology*, vol. 200, no. 1, pp. 28–35, Oct. 2017.

[16] G. Holzapfel, "Chapter 11 Collagen in Arterial Walls : Biomechanical Aspects," 2008.

[17] V. Ayyalasomayajula, B. Pierrat, and P. Badel, “A computational model for understanding the micro-mechanics of collagen fiber network in the tunica adventitia,” *Biomechanics and Modeling in Mechanobiology*, vol. 18, no. 5, pp. 1507–1528, Oct. 2019.

[18] M. D. Rekhter, E. R. Andreeva, A. A. Mironov, and A. N. Orekhov, “Three-dimensional cytoarchitecture of normal and atherosclerotic intima of human aorta.,” *The American Journal of Pathology*, vol. 138, no. 3, p. 569, 1991.

[19] C. K. Chai, A. C. Akyildiz, L. Speelman, *et al.*, “Local anisotropic mechanical properties of human carotid atherosclerotic plaques - Characterisation by micro-indentation and inverse finite element analysis,” *Journal of the Mechanical Behavior of Biomedical Materials*, vol. 43, pp. 59–68, 2015.

[20] G. Antonacci, R. M. Pedrigi, A. Kondiboyina, *et al.*, “Quantification of plaque stiffness by Brillouin microscopy in experimental thin cap fibroatheroma,” *Journal of the Royal Society Interface*, vol. 12, no. 112, 2015.

[21] C. K. Chai, A. C. Akyildiz, L. Speelman, *et al.*, “Local axial compressive mechanical properties of human carotid atherosclerotic plaques-characterisation by indentation test and inverse finite element analysis,” *Journal of Biomechanics*, vol. 46, no. 10, pp. 1759–1766, 2013.

[22] L. A. Davis, S. E. Stewart, C. G. Carsten, B. A. Snyder, M. A. Sutton, and S. M. Lessner, “Characterization of fracture behavior of human atherosclerotic fibrous caps using a miniature single edge notched tensile test,” *Acta Biomaterialia*, vol. 43, pp. 101–111, 2016.

[23] Y. Wang, J. A. Johnson, A. Fulp, M. A. Sutton, and S. M. Lessner, “Adhesive strength of atherosclerotic plaque in a mouse model depends on local collagen content and elastin fragmentation,” *Journal of Biomechanics*, vol. 46, no. 4, pp. 716–722, Feb. 2013.

[24] H. E. Barrett, E. M. Cunnane, E. G. Kavanagh, and M. T. Walsh, “Towards the characterisation of carotid plaque tissue toughness: Linking mechanical properties to plaque composition,” *Acta Biomaterialia*, vol. 43, pp. 88–100, 2016.

[25] S. J. Howell, “Carotid endarterectomy,” *BJA: British Journal of Anaesthesia*, vol. 99, no. 1, pp. 119–131, Jul. 2007.

[26] J. A. Schaar, C. L. De Korte, F. Mastik, and A. F. Van Der Steen, “Effect of temperature increase and freezing on intravascular elastography,” *Ultrasonics*, vol. 40, no. 1-8, pp. 879–881, May 2002.

[27] M. Roffi, D. Mukherjee, and D. G. Clair, “Carotid artery stenting vs. endarterectomy,” *European heart journal*, vol. 30, no. 22, pp. 2693–2704, Nov. 2009.

[28] J. J. Mulvihill and M. T. Walsh, “On the mechanical behaviour of carotid artery plaques: the influence of curve-fitting experimental data on numerical model results,” *Biomechanics and modeling in mechanobiology*, vol. 12, no. 5, pp. 975–985, Oct. 2013.

[29] E. M. Cunnane, H. E. Barrett, E. G. Kavanagh, R. Mongrain, and M. T. Walsh, “The influence of composition and location on the toughness of human atherosclerotic femoral plaque tissue,” *Acta Biomaterialia*, vol. 31, pp. 264–275, Feb. 2016.

[30] B. L. O’Reilly, N. Hynes, S. Sultan, P. E. McHugh, and J. P. McGarry, “An experimental and computational investigation of the material behaviour of discrete homogenous iliofemoral and carotid atherosclerotic plaque constituents,” *Journal of biomechanics*, vol. 106, Jun. 2020.

[31] A. M. Larson, “Multiphoton microscopy,” *Nature Photonics 2011 5:1*, vol. 5, no. 1, pp. 1–1, Dec. 2010.

[32] M. May, *Shedding light on deep tissue: Multiphoton microscopy | Science | AAAS*.

[33] E. E. Van Haaften, T. B. Wissing, M. C. Rutten, *et al.*, “Decoupling the Effect of Shear Stress and Stretch on Tissue Growth and Remodeling in a Vascular Graft,” *Tissue engineering. Part C, Methods*, vol. 24, no. 7, pp. 418–429, Jul. 2018.

[34] P. Berens, “CircStat: A MATLAB Toolbox for Circular Statistics,” *Journal of Statistical Software*, vol. 31, no. 10, pp. 1–21, Sep. 2009.

[35] I. I. Geneva, B. Cuzzo, T. Fazili, and W. Javaid, “Normal Body Temperature: A Systematic Review,” *Open Forum Infectious Diseases*, vol. 6, no. 4, Apr. 2019.

[36] M. Palanca, G. Tozzi, and L. Cristofolini, “The use of digital image correlation in the biomechanical area: a review,” *http://mc.manuscriptcentral.com/tbbe*, vol. 3, no. 1, pp. 1–21, 2015.

[37] C. Wex, S. Arndt, A. Stoll, C. Bruns, and Y. Kupriyanova, “Isotropic incompressible hyperelastic models for modelling the mechanical behaviour of biological tissues: A review,” *Biomedizinische Technik*, vol. 60, no. 6, pp. 577–592, Dec. 2015.

[38] A. Whelan, J. Duffy, R. T. Gaul, *et al.*, “Collagen fibre orientation and dispersion govern ultimate tensile strength, stiffness and the fatigue performance of bovine pericardium,” *Journal of the Mechanical Behavior of Biomedical Materials*, vol. 90, pp. 54–60, Feb. 2019.

[39] T. Khamdaeng, J. Luo, J. Vappou, P. Terdtoon, and E. E. Konofagou, “Arterial stiffness identification of the human carotid artery using the stress–strain relationship in vivo,” *Ultrasonics*, vol. 52, no. 3, pp. 402–411, Mar. 2012.

[40] Z. Teng, Y. Zhang, Y. Huang, *et al.*, “Material properties of components in human carotid atherosclerotic plaques: a uniaxial extension study,” *Acta biomaterialia*, vol. 10, no. 12, pp. 5055–5063, 2014.

[41] J. Blaber, B. Adair, and A. Antoniou, “Ncorr: Open-Source 2D Digital Image Correlation Matlab Software,” *Experimental Mechanics*, vol. 55, no. 6, pp. 1105–1122, Jul. 2015.

[42] A. J. Nederveen, S. Avril, and L. Speelman, “MRI strain imaging of the carotid artery: present limitations and future challenges,” *Journal of biomechanics*, vol. 47, no. 4, pp. 824–833, Mar. 2014.

[43] G. R. Douglas, A. J. Brown, J. H. Gillard, M. R. Bennett, M. P. F. Sutcliffe, and Z. Teng, “Impact of Fiber Structure on the Material Stability and Rupture Mechanisms of Coronary Atherosclerotic Plaques,” *Annals of Biomedical Engineering 2017 45:6*, vol. 45, no. 6, pp. 1462–1474, Mar. 2017.

[44] O. Lisický, A. Hrubanová, R. Staffa, R. Vlachovský, and J. Burša, “Constitutive models and failure properties of fibrous tissues of carotid artery atheroma based on their uniaxial testing,” *Journal of Biomechanics*, vol. 129, p. 110 861, Dec. 2021.

[45] E. Maher, A. Creane, S. Sultan, N. Hynes, C. Lally, and D. J. Kelly, “Tensile and compressive properties of fresh human carotid atherosclerotic plaques,” *Journal of biomechanics*, vol. 42, no. 16, pp. 2760–2767, Dec. 2009.

[46] M. Kobielarz, “Effect of collagen fibre and elastic lamella content on the mechanical behaviour of abdominal aortic aneurysms,” *Acta of Bioengineering and Biomechanics*, vol. 22, no. 3, pp. 1–21, 2020.

[47] J. A. Niestrawska, P. Regitnig, C. Viertler, T. U. Cohnert, A. R. Babu, and G. A. Holzapfel, “The role of tissue remodeling in mechanics and pathogenesis of abdominal aortic aneurysms,” *Acta Biomaterialia*, vol. 88, pp. 149–161, Apr. 2019.

[48] G. A. Holzapfel, “Determination of material models for arterial walls from uniaxial extension tests and histological structure,” *Journal of Theoretical Biology*, vol. 238, no. 2, pp. 290–302, Jan. 2006.

[49] Z. Teng, D. Tang, J. Zheng, P. K. Woodard, and A. H. Hoffman, “An experimental study on the ultimate strength of the adventitia and media of human atherosclerotic carotid arteries in circumferential and axial directions,” *Journal of biomechanics*, vol. 42, no. 15, pp. 2535–2539, Nov. 2009.

[50] E. M. Cunnane, J. J. Mulvihill, H. E. Barrett, M. M. Hennessy, E. G. Kavanagh, and M. T. Walsh, “Mechanical properties and composition of carotid and femoral atherosclerotic plaques: A comparative study,” *Journal of Biomechanics*, vol. 49, no. 15, pp. 3697–3704, Nov. 2016.

[51] H. E. Barrett, K. Van der Heiden, E. Farrell, F. J. Gijsen, and A. C. Akyildiz, “Calcifications in atherosclerotic plaques and impact on plaque biomechanics,” *Journal of biomechanics*, vol. 87, pp. 1–12, Apr. 2019.

[52] C. Sang, S. Maiti, R. N. Fortunato, J. Kofler, and A. M. Robertson, “A Uniaxial Testing Approach for Consistent Failure in Vascular Tissues,” *Journal of biomechanical engineering*, vol. 140, no. 6, Jun. 2018.

6

Appendix

6.0.1. Inflection points

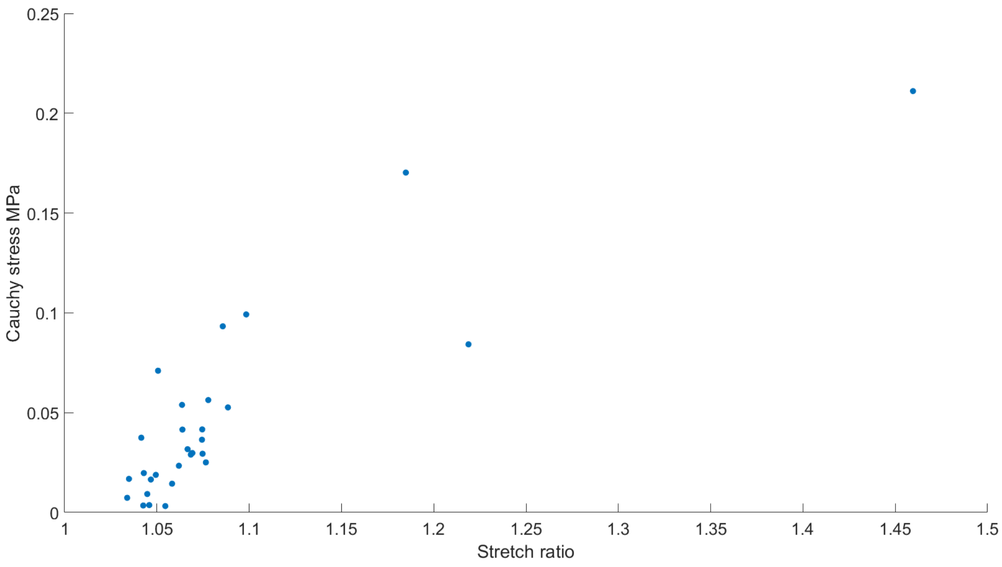

Figure 6.1: Inflection point locations

.

6.0.2. Strip dimension measurements, location of rupture and Ultimate parameters

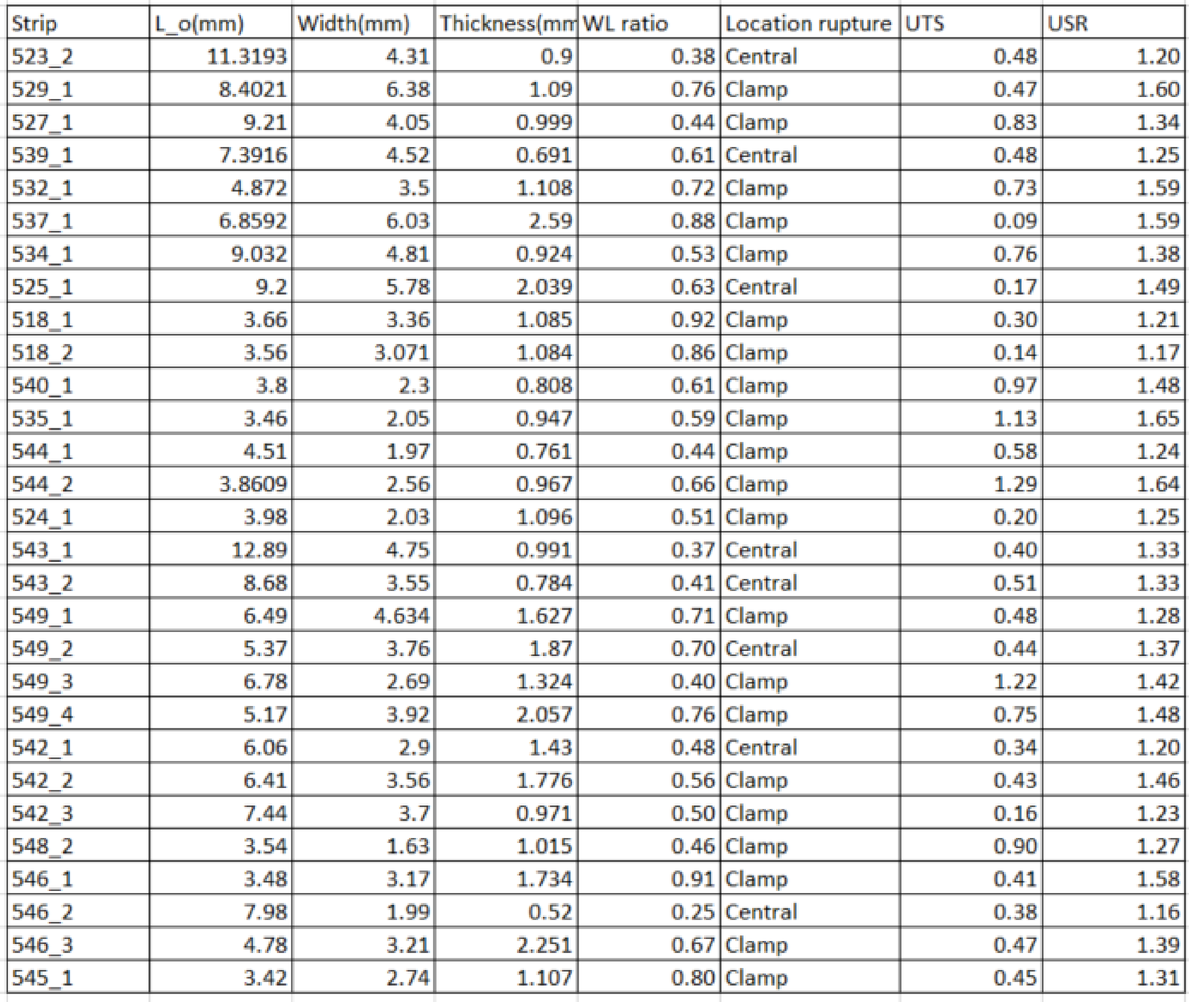

Strip	L_o(mm)	Width(mm)	Thickness(mm	WL ratio	Location rupture	UTS	USR
523_2	11.3193	4.31	0.9	0.38	Central	0.48	1.20
529_1	8.4021	6.38	1.09	0.76	Clamp	0.47	1.60
527_1	9.21	4.05	0.999	0.44	Clamp	0.83	1.34
539_1	7.3916	4.52	0.691	0.61	Central	0.48	1.25
532_1	4.872	3.5	1.108	0.72	Clamp	0.73	1.59
537_1	6.8592	6.03	2.59	0.88	Clamp	0.09	1.59
534_1	9.032	4.81	0.924	0.53	Clamp	0.76	1.38
525_1	9.2	5.78	2.039	0.63	Central	0.17	1.49
518_1	3.66	3.36	1.085	0.92	Clamp	0.30	1.21
518_2	3.56	3.071	1.084	0.86	Clamp	0.14	1.17
540_1	3.8	2.3	0.808	0.61	Clamp	0.97	1.48
535_1	3.46	2.05	0.947	0.59	Clamp	1.13	1.65
544_1	4.51	1.97	0.761	0.44	Clamp	0.58	1.24
544_2	3.8609	2.56	0.967	0.66	Clamp	1.29	1.64
524_1	3.98	2.03	1.096	0.51	Clamp	0.20	1.25
543_1	12.89	4.75	0.991	0.37	Central	0.40	1.33
543_2	8.68	3.55	0.784	0.41	Central	0.51	1.33
549_1	6.49	4.634	1.627	0.71	Clamp	0.48	1.28
549_2	5.37	3.76	1.87	0.70	Central	0.44	1.37
549_3	6.78	2.69	1.324	0.40	Clamp	1.22	1.42
549_4	5.17	3.92	2.057	0.76	Clamp	0.75	1.48
542_1	6.06	2.9	1.43	0.48	Central	0.34	1.20
542_2	6.41	3.56	1.776	0.56	Clamp	0.43	1.46
542_3	7.44	3.7	0.971	0.50	Clamp	0.16	1.23
548_2	3.54	1.63	1.015	0.46	Clamp	0.90	1.27
546_1	3.48	3.17	1.734	0.91	Clamp	0.41	1.58
546_2	7.98	1.99	0.52	0.25	Central	0.38	1.16
546_3	4.78	3.21	2.251	0.67	Clamp	0.47	1.39
545_1	3.42	2.74	1.107	0.80	Clamp	0.45	1.31

Figure 6.2: Dimensions, location of rupture, Ultimate tensile strength and Ultimate stretch ratio of the strips succesfully tested under uniaxial tensile testing.

.

6.0.3. Interpolation maps of strips

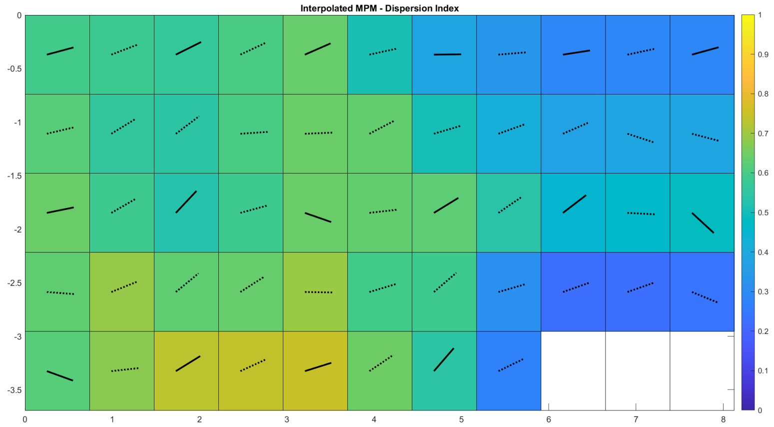

Figure 6.3: Interpolation map of sample 518-1 representing $\mu_p$and DI

.

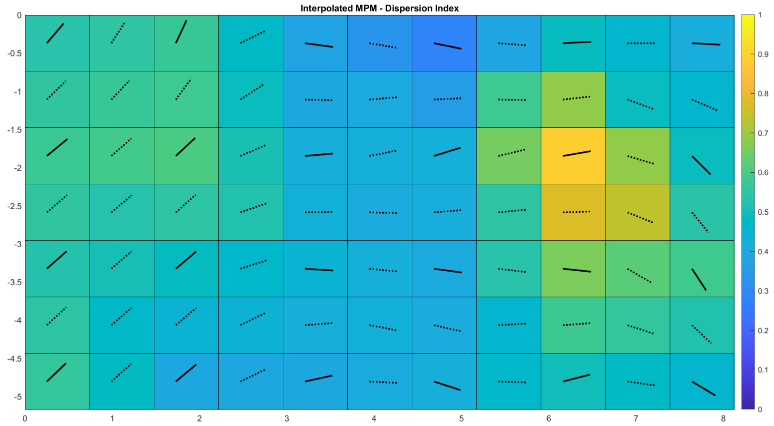

Figure 6.4: Interpolation map of sample 525-1 representing $\mu_p$and DI

.

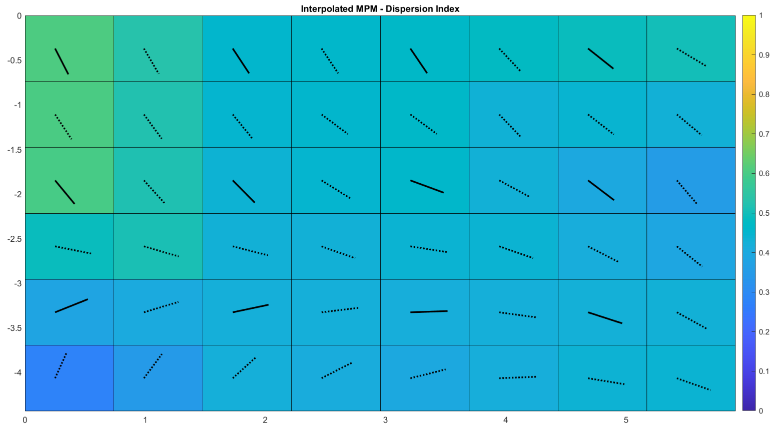

Figure 6.5: Interpolation map of sample 539-1 representing $\mu_p$and DI

.

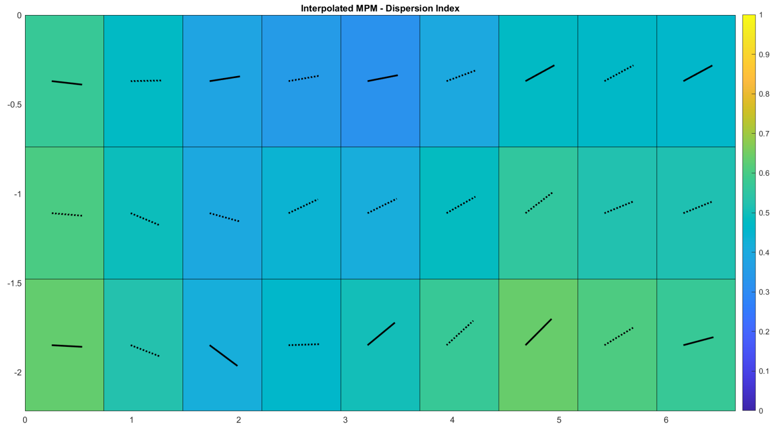

Figure 6.6: Interpolation map of sample 540-1 representing $\mu_p$and DI

.

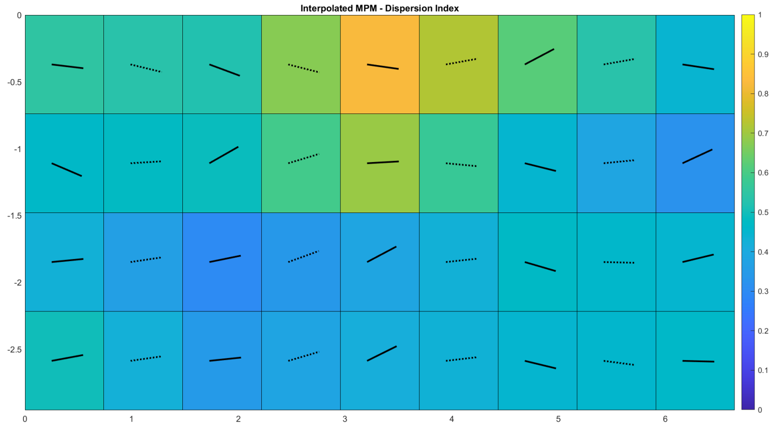

Figure 6.7: Interpolation map of sample 542-1 representing $\mu_p$and DI

.

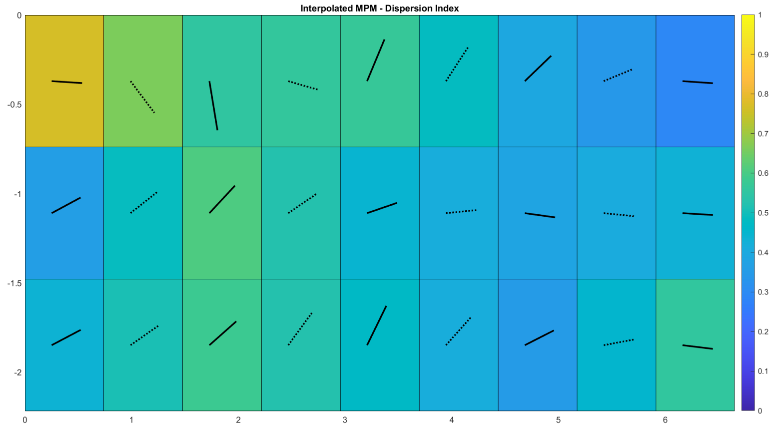

Figure 6.8: Interpolation map of sample 546-2 representing $\mu_p$and DI

.

6.0.4. DIC-based tensile strains at the physiological frame

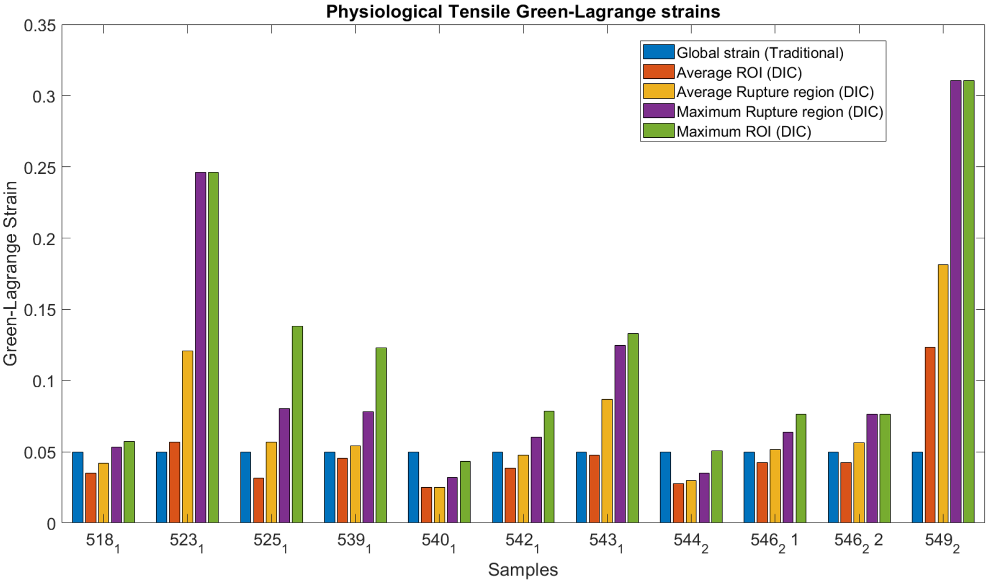

Figure 6.9: Green-Lagrange tensile strains at the physiological frame for all samples analyzed: Blue: Global strain at rupture initiation from (GL-based). Orange: Average strain of whole ROI (DIC-based). Yellow: Average strain at the rupture region (RR) (DIC-based). Purple: Maximum value of strain at the Rupture region (DIC-based). Green: Maximum value of strain at the whole ROI (DIC-based).

.

6.0.5. High local strains at the near-clamp regions

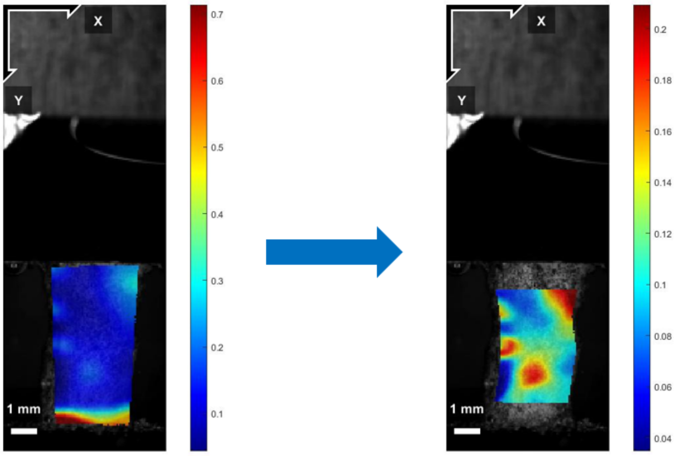

Figure 6.10: Left)DIC strain distribution maps at the Rupture frame showing the high strains at the near rupture region compared to the central part of the region. Right) DIC strain distribution of a ROI where near-clamp areas (1mn) have been excluded, as in the analysis presented in the 3.12

.